THE ASTRONOMICAL JOURNAL, 121:2331–2357, 2001 May
© 2001. The American Astronomical Society. All rights reserved. Printed in U.S.A.

THE FIRST HOUR OF EXTRAGALACTIC DATA OF THE SLOAN DIGITAL SKY SURVEY SPECTROSCOPIC COMMISSIONING: THE COMA CLUSTER

FRANCISCO J. CASTANDER,[1,2,3,4] ROBERT C. NICHOL,[5] ARONNE MERRELLI,[5,6] SCOTT BURLES,[1,7] ADRIAN POPE,[5,8] ANDREW J. CONNOLLY,[9] ALAN UOMOTO,[8] JAMES E. GUNN,[10] JOHN E. ANDERSON,[7] JAMES ANNIS,[7] NETA A. BAHCALL,[10] WILLIAM N. BOROSKI,[7] JON BRINKMANN,[11] LARRY CAREY,[12] JAMES H. CROCKER,[8] ISTVÁN CSABAI,[8,13] MAMORU DOI,[14] JOSHUA A. FRIEMAN,[1,7] MASATAKA FUKUGITA,[15,16] SCOTT D. FRIEDMAN,[8] ERIC J. HILTON,[5] ROBERT B. HINDSLEY,[17] ŽELJKO IVEZIĆ,[10] STEVE KENT,[7] DONALD Q. LAMB,[1] R. FRENCH LEGER,[12] DANIEL C. LONG,[11] JON LOVEDAY,[18] ROBERT H. LUPTON,[10] HARVEY MACGILLIVRAY,[19] AVERY MEIKSIN,[19] JEFFREY A. MUNN,[20] MATT NEWCOMB,[5] SADANORI OKAMURA,[14] RUSSELL OWEN,[12] JEFFREY R. PIER,[20] CONSTANCE M. ROCKOSI,[1] DAVID J. SCHLEGEL,[10] DONALD P. SCHNEIDER,[21] WALTER SEIGMUND,[12] STEPHEN SMEE,[8] YEHUDA SNIR,[5] LARRY STARKMAN,[12] CHRIS STOUGHTON,[7] GYULA P. SZOKOLY,[22] CHRISTOPHER STUBBS,[12] MARK SUBBARAO,[1] ALEX SZALAY,[8] ANIRUDDHA R. THAKAR,[8] CHRISTY TREMONTI,[8] PATRICK WADDELL,[12] BRIAN YANNY,[7] AND DONALD G. YORK[1]

Received 2000 October 24; accepted 2001 January 29

ABSTRACT

On 1999 May 26, one of the Sloan Digital Sky Survey (SDSS) fiber-fed spectrographs saw astronomical first light. This was followed by the first spectroscopic commissioning run during the dark period of 1999 June. We present here the first hour of extragalactic spectroscopy taken during these early commissioning stages: an observation of the Coma cluster of galaxies. Our data samples the southern part of this cluster, out to a radius of 1.°5 (1.8 h^{-1} Mpc, approximately to the virial radius) and thus fully covers the NGC 4839 group. We outline in this paper the main characteristics of the SDSS spectroscopic systems and provide redshifts and spectral classifications for 196 Coma galaxies, of which 45 redshifts are new. For the 151 galaxies in common with the literature, we find excellent agreement between our redshift determinations and the published values, e.g., for the largest homogeneous sample of galaxies in common (63 galaxies observed by Colless & Dunn) we find a mean offset of 3 km s^{-1} and an rms scatter of only 24 km s^{-1}. As part of our analysis, we have investigated four different spectral classification algorithms: measurements of the spectral line strengths, a principal component decomposition, a wavelet analysis and the fitting of spectral synthesis models to the data. We find that these classification schemes are in broad agreement and can provide physical insight into the evolutionary histories of our cluster galaxies. We find that a significant fraction (25%) of our observed Coma galaxies show signs of recent star formation activity and that the velocity dispersion of these active galaxies (emission-line and poststarburst galaxies) is 30% larger than the absorption-line galaxies. We also find no active galaxies within the central (projected) 200 h^{-1} kpc of the cluster. The spatial distribution of our Coma active galaxies is consistent with that found at higher redshift for the CNOC1 cluster survey. Beyond the core region, the fraction of bright active galaxies appears to rise slowly out to the virial radius and are randomly distributed within the cluster with no apparent correlation with the potential merger or postmerger of the NGC 4839 group. We briefly discuss possible origins of this recent galaxy star formation.

Key words: catalogs — cosmology: observations — galaxies: clusters: individual (Coma) — galaxies: fundamental parameters — methods: data analysis

[1] Astronomy and Astrophysics Center, University of Chicago, 5640 South Ellis Avenue, Chicago, IL 60637.
[2] Observatoire Midi-Pyrénées, 14 avenue Edouard Belin, Toulouse, F-31400, France.
[3] Current address:Yale University, P.O. Box 208101, New Haven, CT 06520; Universidad de Chile, Casilla 36-D, Santiago, Chile.
[4] Andes Fellow.
[5] Department of Physics, Carnegie Mellon University, 5000 Forbes Avenue, Pittsburgh, PA 15232.
[6] Department of Astronomy, California Institute of Technology, Pasadena, CA 91125.
[7] Fermi National Accelerator Laboratory, P.O. Box 500, Batavia, IL 60510.
[8] Department of Physics and Astronomy, Johns Hopkins University, 3701 San Martin Drive, Baltimore, MD 21218.
[9] Department of Physics and Astronomy, University of Pittsburgh, Pittsburgh, PA 15260.
[10] Princeton University Observatory, Princeton, NJ 08544.
[11] Apache Point Observatory, P.O. Box 59, Sunspot, NM 88349-0059.
[12] Department of Astronomy, University of Washington, Box 351580, Seattle, WA 98195.
[13] Department of Physics of Complex Systems, Eötvös Loránd University, Pázmány Péter sétány 1/A, H-1117 Budapest, Hungary.
[14] Department of Astronomy and Research Center for the Early Universe, School of Science, University of Tokyo, Hongo, Bunkyo, Tokyo, 113-0033, Japan.
[15] Institute for Cosmic-Ray Research, University of Tokyo, Midori, Tanashi, Tokyo 188-8502, Japan.
[16] Institute for Advanced Study, Olden Lane, Princeton, NJ 08540.
[17] Remote Sensing Division, Naval Research Laboratory, 4555 Overlook Avenue, SW, Washington, DC 20375.
[18] Astronomy Center, University of Sussex, Falmer, Brighton BN1 9QJ, England, UK.
[19] Royal Observatory, Edinburgh, EH9 3HJ, England, UK.
[20] US Naval Observatory, Flagstaff Station, P.O. Box 1149, Flagstaff, AZ 86002-1149.
[21] Department of Astronomy and Astrophysics, Pennsylvania State University, University Park, PA 16802.
[22] Astrophysikalisches Institut Potsdam, An der Sternwarte 16, D-14482 Potsdam, Germany.

1. INTRODUCTION

The Coma cluster is the richest cluster of galaxies in our local universe and has thus attracted considerable attention over the last century (see reviews by Biviano 1998 and West 1998). In the optical, for example, Goldwin, Metcalfe, & Peach (1983; hereafter GMP83) have published an extensive photometric study of the cluster providing accurate positions, colors, magnitudes and ellipticities for 6724 bright galaxies over 2.63 deg^2 centered on Coma. Several authors have explored the fainter dwarf galaxy population of Coma (see Bernstein et al. 1995; Kashikawa et al. 1998; Adami et al. 1998 and 2000). The dynamics of the cluster have also been well studied. Kent & Gunn (1982) assembled approximately 300 optical redshifts from the literature to determine the cluster mass distribution. This initial work was extended by Colless & Dunn (1996, hereafter CD96), who collected 556 redshifts (based on new and literature redshifts), and Geller, Diaferio, & Kurtz (1999) who have extended the dynamical study of Coma to large radii (10°) and larger numbers (1693 redshifts), thus measuring the density profile of Coma well beyond the virial radius of the cluster. Hughes (1989) measured the total mass of Coma using early X-ray observations of the cluster. More recently, *ROSAT* observations of Coma have provided unprecedented detail of the intracluster gas morphology (e.g., Briel, Henry, & Böhringer 1992; White, Briel, & Henry 1993). *ASCA* observations of the cluster have provided important information on the temperature structure of the X-ray emitting gas (Honda et al. 1996) which have been recently complemented by XMM-Newton observations (Briel et al. 2001; Arnaud et al. 2001; Neumann et al. 2001)

The Coma cluster has long been regarded as the archetypal relaxed massive cluster of galaxies. However, recent studies of the cluster have shown otherwise. The current view of Coma is that the cluster is the product of one recent and one ongoing cluster-group merger. A group centered on NGC 4839, in the southwest region of the cluster, is falling into (CD96), or has just passed through (Burns et al. 1994), the main body of the cluster and may have triggered new star formation in galaxies in Coma (Caldwell & Rose 1997). The velocity dispersion of this southwest group is approximately $\frac{1}{3}$ of that of the main cluster. Meanwhile, the core of Coma has two dominant galaxies, NGC 4874 and NGC 4889, which seem to be the relic central galaxies of previous groups that have recently merged into the current cluster. The X-ray and dynamical data reveal that neither of these dominant galaxies appear to sit at the bottom of the cluster potential (CD96; White, Briel, & Henry 1993). The lack of a cooling flow and the existence of an extended radio halo support this merging history of the cluster.

The Coma cluster was thus an ideal first target for the Sloan Digital Sky Survey (SDSS; York et al. 2000) spectroscopic commissioning program because of its location (the north Galactic pole), the preexistence of wide-field galaxy photometry (e.g., GMP83), and the high density of known redshifts for comparison and testing. Moreover, there remains interesting scientific questions that can be addressed using the unique SDSS spectroscopic hardware e.g., the influence of cluster merger events on the star formation rates of galaxies. The quality and quantity of SDSS spectral data will allow us to study such problems in great detail and in this paper, we start by outlining and comparing the different analysis techniques for classifying SDSS galaxy spectra as well as quantifying their star formation rates.

Robust, automated, spectral classification methods are necessary to help us understand the distribution and evolution of the galaxies physical properties that define and characterize their spectral energy distributions. The problem of galaxy spectra classification has been copiously treated in the astronomical literature. In general, methods are based on the measurement of spectral continuum and line features (e.g., the Lick/IDS system, Faber et al. 1985; Burstein, Faber, & González 1986) which are then used to classify and derive the galaxies physical properties. Stellar population synthesis models can, for example, be compared with these measurements, or the entire spectrum using template fitting, to provide a physical understanding of the galaxy properties. Recently, other techniques have been investigated. Amongst them, the principal component analysis has attracted a lot of interest (e.g., Connolly et al. 1995; Bromley et al. 1998; Folkes et al. 1999; Ronen, Aragón-Salamanca, & Lahav 1999). The technique is based on decomposing the spectra into a basis that highlights the galaxy differences. Such decomposition can therefore be used to classify the spectra. Different implementations change the way the basis is constructed or how the resulting coefficients of the decomposition are used to generate a classification method. Some authors, for instance, use artificial neural networks to build a classification scheme from the principal component coefficients (e.g., Folkes, Lahav, & Maddox 1996). Wavelets also provide an orthogonal basis in which the spectra can be decomposed and therefore can in principle be used as a classification method. Along these lines, Pando & Fang (1996) and Theuns & Zaroubi (2000) have used wavelets to study quasar spectra.

In this paper, we present the first hour of extragalactic data taken by the SDSS spectroscopic system. Only one of the ten plates originally designed in the Coma region has been observed producing nearly 200 Coma redshifts and thus illustrating the capabilities of this new instrumentation. These spectra will allow us to investigate several classification schemes and test their applicability to the future SDSS data set. The paper is structured as follows. In § 2, we briefly highlight the main characteristics of the SDSS spectroscopic system. In § 3, we describe the selection of galaxy targets in the Coma cluster region. The observations of the Coma cluster plates are presented in § 4. In § 5, we describe the data analysis. We discuss the redshift measurements in § 6 and classify the galaxy members in § 7. Finally, we discuss our data and present our conclusions in § 8.

2. THE SDSS SPECTROSCOPIC SYSTEM

The SDSS will use a dedicated 2.5 m telescope with a 3° field of view and two fiber-fed double spectrographs to measure the redshifts of approximately a million galaxies and one hundred thousand quasars over the next 5 years. The SDSS will also image the same area of the sky to an approximate depth of $\sim$23 mag in five optical bands (u', g', r', i', and z'; Fukugita et al. 1996; Fan et al. 2000). For more details on the SDSS, the reader is referred to York et al. 2000 for a brief overview of the survey hardware, software, and strategy.[23] The full details of the SDSS spectroscopic

[23] In addition, the reader can refer to the on-line SDSS Project Book at http://www.astro.princeton.edu/PBOOK/welcome.html.

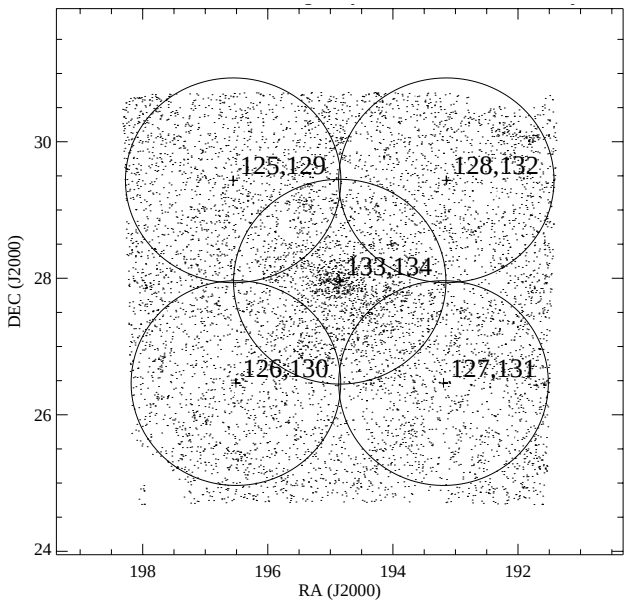


FIG. 1.—Distribution of SuperCOSMOS galaxies in the Coma cluster region. The circles superposed on the data show the position of our 10 designed plug plates. We designed two plates at each position: one containing the brighter sources, the other fainter sources. The numbers are the SDSS plate identifiers. Because of engineering and weather constraints during the commissioning period in 1999 June, only plate 133 was observed.

system will be presented in Uomoto et al. (2001) and Frieman et al. (2001). For completeness, we provide here an outline of the SDSS spectroscopic system.

The SDSS spectrographs are designed to cover the wavelength range of $3900 \rightarrow 9100$ Å. This is achieved using a dichroic beam splitter centered at $\simeq 6000$ Å to separate the incoming light onto a red and blue camera in both spectrographs. The SDSS spectrographs achieve a spectral resolution of 1800 across its entire spectral range. Each spectrograph accepts 320 fibers, each of which subtends a diameter of 3″ on the sky. The fibers are plugged into aluminum plug plates sitting in the focal plane of the SDSS telescope. Each plate contains 640 science holes (one for each science fiber), light-trap holes (drilled to avoid the reflection of light from bright stars off the plug plate back into the telescope optics), guide star holes (11 in total which are fed to the guide camera), and quality assurance holes.

During normal operations, plates scheduled for observation are manually plugged during the day. Each plug plate is mounted in an individual cartridge that possesses a full set of 640 science fibers and 11 coherent fiber bundles that are plugged into the guide star holes and used to guide the telescope. Once plugged, the cartridges are automatically mapped with a video system that measures the plug-plate location of each fiber (i.e., sky coordinates) as they are successively illuminated by a laser diode at the slit head. After mapping the cartridges are ready to be mounted on the SDSS telescope during the night.

3. TARGET SELECTION

In normal survey operations, the SDSS selects targets for spectroscopic observation using the SDSS photometric survey. However, in the case of the Coma cluster, the SDSS imaging photometric camera had not yet observed this region of the sky and thus target selection was performed using an external catalog.

We have used the SuperCOSMOS scans of two photographic plates (J and O), centered on the Coma cluster,[24] kindly provided to us by H. MacGillivray. The passband of the J plate is the combination of the Kodak IIIaJ emulsion and a GG395 filter (same as the UK Schmidt b_j system; see Nichol, Collins, & Lumsden 2000), while the passband of the O plate is the combination of the IIIaF emulsion and a OG590 filter. The raw object lists of these two SuperCOSMOS scans contain approximately 150,000 objects per plate and therefore must be trimmed for our purposes.

We first merged the two photographic plates catalogs keeping only objects that matched to within 1.″5. This merged catalog was separated into a list of stars and galaxies using the SuperCOSMOS source classifier. We produced two lists; one of stellar sources, which were objects classified as stars on both plates, and one of galaxies, which were objects classified as galaxies on at least one of the plates. We used these criteria since star-galaxy separation becomes increasingly difficult at the fainter magnitudes. By including sources which were classified as a galaxy in one plate, but as a star in the other, we hoped to recover some of the faint galaxy population that would have otherwise been missed. Unfortunately, we can expect a higher stellar contamination (especially from blended stars) in our galaxy list compared with only selecting targets classified as galaxies on both plates.

We photometrically calibrated the SuperCOSMOS data using the GMP83 catalog. We matched our galaxy list to the GMP83 data and then derived a transformation to convert the SuperCOSMOS instrumental magnitudes into

[24] Details available at http://www-wfau.roe.ac.uk/sss.

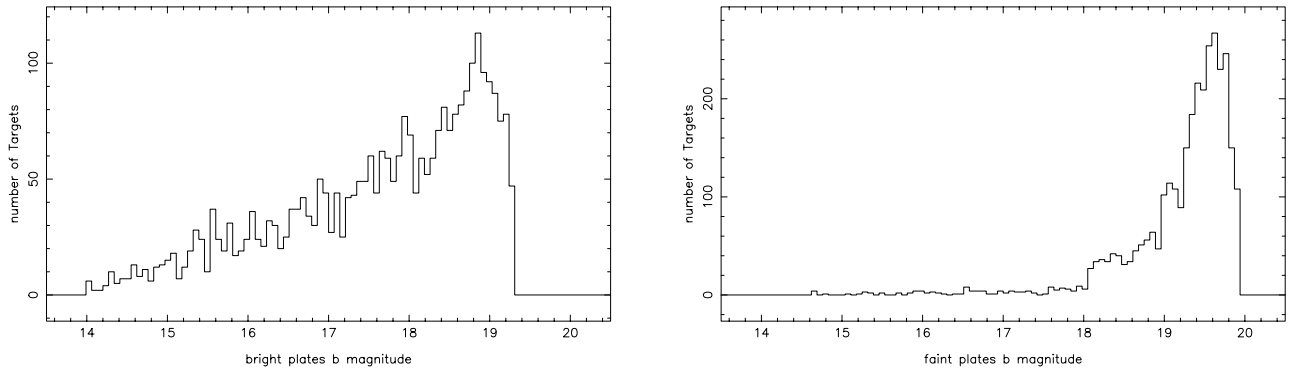


FIG. 2.—Magnitude distribution of selected sources in the five *bright* plates (*top*) and the five *faint* plates (*bottom*)

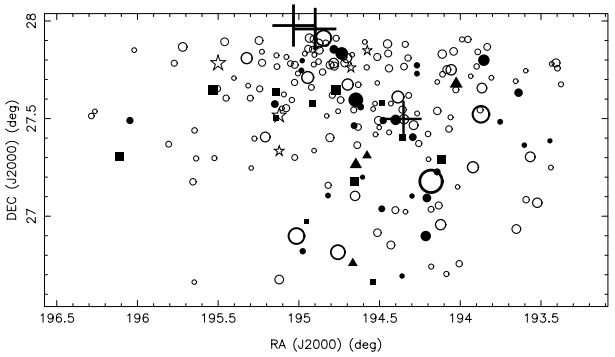


FIG. 3.—Distribution on the sky of the observed Coma galaxies. All galaxy spectra were obtained with the central bright Coma plate (No. 133). Note the semicircle shape sampling due to the availability of only one spectrograph. The different symbols represent different galaxy types: AB (*open circles*); AB+EM (*solid circles*); EM+AB (*solid squares*); EM (*solid triangles*); PS (*stars*) (see text). The position of NGC4874, NGC4889, and NGC4839 are also shown as plus signs. The size of the symbols denotes the b magnitude of the object, from the brightest (*largest symbol*) $b = 14.0$, to the faintest (*smallest*) $b = 18.0$, excluding the plus signs.

the GMP83 magnitude system which was calibrated using B-band photoelectric magnitudes for their blue band and $B-R$ colors for their red band (see GMP83 for details). Our photometry is thus measured in the blue and red "photographic bands" (emulsion + filter described above), but transformed to the GMP83 system with a zero-point and color terms. Hereafter, we will refer to these magnitudes as, b and r, following the notation in GMP83. Finally, a small astrometric correction was applied by correlating our star catalog with the ACT star reference catalog.[25]

The resulting list of galaxies contained nearly 33,000 objects. This was further trimmed to 8187 targets by imposing a magnitude cut of $14 \leq b \leq 20$. From these targets, a total of 10 plates were designed, with two plates at each of the five plate centers shown in Figure 1. Each pair of plates was allocated unique targets, with one plate containing the brighter galaxies and the other containing the fainter galaxies (see Fig. 2). This was done for two reasons; first, to accommodate the minimum spacing restriction between SDSS fibers (55″) and, second, to allow for different exposure times for these plates. Finally, each plate was allocated a set of 10 bright stars ($14 < b < 15$) for the guide camera fibers. Since these were selected from the same Super-COSMOS data there was little concern about their relative astrometric reference frame.

4. OBSERVATIONS

One of the SDSS spectrographs saw first astronomical light on 1999 May 26 in bright time. After this milestone, the first spectroscopic commissioning run took place in the dark period of 1999 June. At the time of the Coma SDSS spectroscopic observations, several parts of the nominal SDSS spectroscopic system were either not available or were being commissioned for the first time. For example, only one of the two SDSS spectrographs was mounted on the back of the telescope. Therefore, only 320 science fibers were available per plate, instead of the 640 which is now the standard number. In addition, the plate mapper, which automatically matches the plugged fibers to the target catalog, was not fully automated and we were forced to map the plate by hand. The telescope was not properly collimated at the time of the observations and the hardware needed to obtain spectroscopic calibrations was not installed. Finally, condensation on the front of the red camera dewar produced a series of bright "doughnuts" in the center of the red CCD images, rendering most of the red spectrograph data in this commissioning run almost impossible to use.

On June 6, the SDSS observed plate 133 (the bright plate at the center of Coma). We took two 900 s exposures at mean air masses of 1.53 and 1.66 without guiding. On June 8, plate 133 was reobserved taking three 1200 s exposures. These were the first astronomical exposures in which the SDSS spectroscopic system guided on the sky. The seeing was between 1.″2 and 1.″5 and the mean air masses were 1.07, 1.10, and 1.15 for the three exposures. Being near the zenith, the atmospheric differential refraction effects were small. In addition to plate 133, we also observed plates 135 and 136 on 1999 June 8, which were designed using SDSS photometry in areas of the sky unrelated to the Coma cluster and are thus more representative of the field galaxy population.

Plate 133 is the only Coma plate that has been observed during the SDSS spectroscopic commissioning phase. Figure 3 shows the distribution on the sky of the identified cluster members in this plate. Coma will be reobserved as part of the main SDSS spectroscopic and photometric survey in the coming years. These data will be far superior to the data discussed herein.

5. DATA REDUCTION

In normal production mode the SDSS will reduce the spectroscopic data through a specifically designed pipeline (Frieman et al. 2001). However, due to the uniqueness of these observations and the nonstandard observing setup, the Coma observations were processed using a modified version of an earlier copy of the spectroscopic pipeline. The reduction stages are, nevertheless, standard in multifiber spectroscopy. The blue and red camera data were reduced separately, given the aforementioned problem with the red camera.

First, we subtracted the bias signal using the overscan columns at the edge of the CCD and co-added the individual two-dimensional images, rejecting cosmic rays in the process. We then traced the fibers and optimally extracted the one-dimensional spectra using the Horne (1986) algorithm. In the red this procedure had to be individually supervised and sometimes changed for troublesome fibers. No flat fielding of the data was possible given the lack of uniformly illuminated exposures either for the whole CCD (two-dimensional flat) or through the fibers (one-dimensional flat). We wavelength-calibrated the spectra using the sky emission lines. In the blue, we used the Hg, [O I], and NaD lines, while in the red, we used the numerous OH lines as well. We fitted a third-order polynomial to the wavelength dispersion, and in the blue we obtained residuals of <0.1 Å for most fibers. For a few fibers, we did witness residuals of 0.2 Å (which is $\simeq 15$ km s^{-1}). However, these errors are computed at the position of the skylines and are therefore probably underrepresentative of the wavelength calibration error for the whole spectrum (see below). We obtained a similarly accurate wavelength solution in the

[25] The ACT catalog is produced by the US Naval Observatory; see http://aries.usno.navy.mil/ad/act/act.html.

red. On average, the blue spectra spanned the wavelength range 3770 to 6100 Å with a median dispersion of 1.14 Å pixel^{-1}, while in the red we obtained a wavelength coverage of 5770 to 9120 Å with a median dispersion of 1.64 Å pixel^{-1}. These are close to the original design specification.

To sky-subtract the spectra, we combined the dedicated sky fibers into one "supersky" spectrum which was rebinned to the resolution of the individual spectra and scaled to match the flux of the [O I] λ5577 night skyline of each science fiber to compensate for any fiber throughput differences. Then each rescaled "supersky" was subtracted from the corresponding science fiber. As we did not possess calibration frames, and given the poorer quality of the red side, we did not attempt to merge the red and blue spectra. For the rest of the paper, except on the galaxy classification in § 7 when we use Hα, we only use the blue camera data.

To correct for the intrinsic response of the instrument in the blue, we have used bright, early-type stars observed as part of plate 133. This was achieved by selecting all stars of a spectral type earlier (hotter) than K0, which possessed a signal-to-noise ratio per pixel of greater than 100 at 5000 Å. In total, this criterion provided 15 stars, the earliest type being a A9–F0 star, the latest a K0. We divided these stars by the best-fit stellar template in the Jacoby et al. (1984) stellar atlas. We smoothed, normalized, and combined the resulting spectra to obtain the response function of the instrument. We then divided all the spectra by this response function. We note this procedure does not provide an absolute spectrophotometric calibration; it only corrects for the response function of the instrument.

6. REDSHIFT DETERMINATIONS

We first determined the redshifts of our spectra via visual inspection and fitted Gaussians to all obvious absorption/emission lines. The main absorption lines used were Ca II H and K $\lambda\lambda$3968, 3934, Ca I λ4227, the Balmer series lines, Mg I $\lambda\lambda$5167, 5173, 5184 and NaD $\lambda\lambda$5790, 5796. In emission we used [O II] $\lambda\lambda$3726, 3729, the Balmer series lines and [O III] $\lambda\lambda$4959, 5007. Our visual inspections of the spectra revealed 196 galaxies in the Coma cluster, 49 field galaxies, five quasars, 47 stars, and 12 spectra that could not be classified. The remaining 11 fibers were sky fibers.

We also used the cross-correlation technique to obtain a more accurate galaxy redshift. We utilized the RVSAO package (Kurtz & Mink 1998) within the IRAF environment. Given that the majority of synthetic spectra have resolution coarser than our data, we decided to construct our own templates for the cross-correlation using the stellar objects observed on plate 133; this ensures that we have the same resolution for both the template and object spectra. We chose to use as templates the fifteen stars discussed above (for correcting the response function of the instrument) as well as two additional later-type stars (K1 and K4) that also passed the aforementioned signal-to-noise criterion. We also added emission lines to these stellar templates creating a set of 34 templates, i.e., 17 absorption line stars and 17 absorption and emission stellar templates. All templates were shifted to their rest frame.

To determine the true error on our wavelength solutions and thus our redshifts, we first recalculated the wavelength solution for each of our stellar templates using at least nine absorption lines, and normally 14, per spectrum. The availability of more lines and the better sampling of the wavelength range allowed us to improve the wavelength solution compared with that derived from just the skylines alone. We then cross-correlated these recalibrated stellar templates against higher quality stellar spectra taken by the SDSS in later commissioning observations in the spring of 2000. From these tests, we estimated that our dispersion solutions had an error of $\simeq 30$ km s^{-1} which we added in quadrature to the error resulting from the cross-correlation technique.

In Figure 4, we present the redshift distribution of the 245 galaxies for which we obtained a redshift on plate 133. The Coma cluster can be clearly seen as the broad peak around $z = 0.0232$. Figure 5 is an expanded view of this region together with a 3 σ clipped Gaussian fit to the data. Cluster membership is easily assigned for our galaxy sample since there is only one galaxy in the 3 to 4 σ region of the distribution. This galaxy would not normally be assigned to the cluster based on our data alone, however, CD96 measured a higher number of galaxy redshifts obtaining a larger velocity dispersion which would put this galaxy inside our 3 σ cut. Therefore, for the rest of our analysis, we have included this galaxy as a cluster member, bringing the total number of Coma member on plate 133 to 196.

Table 1 lists the main galaxy data on our Coma galaxies. Column (1) gives the extraction identification number

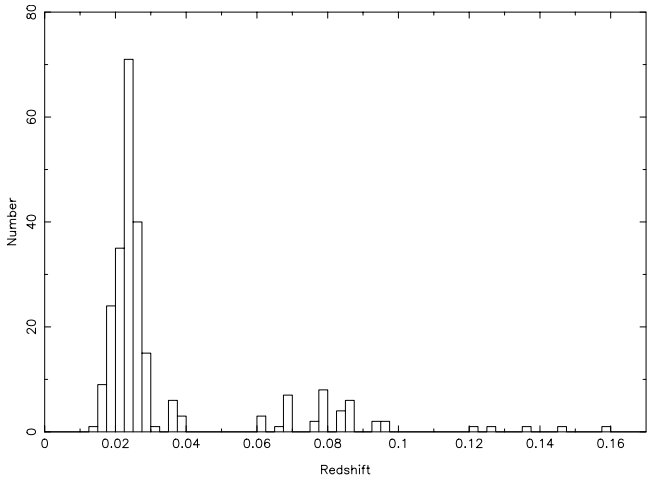


FIG. 4.—Redshift distribution of the all identified galaxies in plate 133

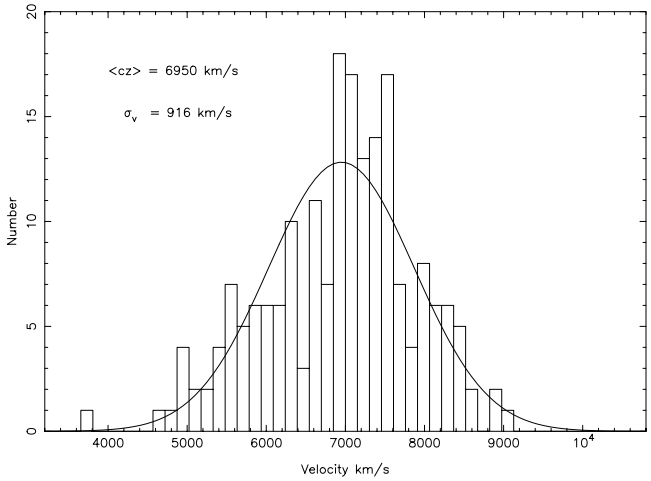


FIG. 5.—Redshift distribution of the Coma galaxies in plate 133

TABLE 1

GALAXY REDSHIFTS

Fiber No. (1)	GMP83 Number (2)	R.A.[a] (3)	Decl.[a] (4)	cz (km s^{-1}) (5)	$\delta\ cz$ (km s^{-1}) (6)	R (7)	b (8)	r (9)
3.....	1411	13 02 32.8	27 17 43	7585	39	6.9	17.36	15.47
4.....	1382	13 02 35.6	26 39 43	7372	72	3.0	17.97	16.04
10	1060	13 03 13.7	27 22 08	6371	32	15.7	16.84	14.88
11	1368	13 02 37.4	27 10 34	5497	33	15.4	16.52	14.65
12	455	13 04 26.6	27 18 16	5534	31	16.9	15.77	14.52
13	1392	13 02 35.2	27 26 20	5400	41	7.4	17.07	15.43
14	1635	13 02 5.5	27 17 50	7258	35	10.5	17.50	15.57
21	1245	13 02 52.7	27 51 59	8207	32	19.9	15.62	13.81
27	1134	13 03 5.2	27 47 03	7671	32	18.9	16.74	14.88
28	177	13 05 8.5	27 30 46	7177	35	10.9	17.05	15.25
29	631	13 04 4.8	27 51 01	6360	34	11.4	17.77	15.96
30	228	13 05 3.3	27 32 13	6603	61	4.3	17.88	16.21
31	1616	13 02 7.9	27 38 54	6915	33	12.4	15.45	13.74
32	1673	13 02 1.1	27 39 10	7065	32	17.6	16.61	14.70
34	595	13 04 11.2	27 29 25	5317	34	10.3	16.50	14.67
40	2235	13 01 10.7	27 14 47	6226	46	5.7	18.01	16.18
43	2278	13 01 6.2	27 23 52	8109	33	14.4	17.42	15.60
45	2639	13 00 29.2	27 19 59	8408	67	5.6	17.67	16.37
50	2643	13 00 29.2	26 40 31	7185	31	23.3	15.60	13.71
55	2431	13 00 49.9	27 24 20	6569	32	16.0	15.32	13.42
58	1681	13 02 0.1	27 46 57	7111	36	12.2	16.08	14.43
61	1961	13 01 36.5	27 42 28	7912	37	8.4	18.03	16.24
65	1832	13 01 48.4	27 36 14	8210	32	17.0	16.70	14.82
66	2219	13 01 12.3	27 36 16	7543	32	17.9	16.79	14.87
68	2385	13 00 54.8	27 50 31	7096	33	13.2	17.68	15.89
69	2157	13 01 17.6	27 48 33	7281	32	20.1	15.04	13.12
70	2347	13 00 59.3	27 53 59	6883	32	19.7	15.88	13.98
74	2355	13 00 58.4	27 39 07	5202	38	6.6	16.67	14.80
75	1807	13 01 50.2	27 53 36	7562	36	10.9	15.89	14.00
76	2185	13 01 15.2	27 40 09	7065	43	7.4	17.76	15.91
84	3143	12 59 49.3	26 58 27	7072	32	13.6	17.88	16.53
85	3618	12 59 16.7	27 06 21	8412	33	13.7	17.38	15.48
86	3622	12 59 16.4	27 09 29	6692	32	17.6	16.67	14.78
87	3310	12 59 37.4	27 20 09	6953	34	11.4	17.84	15.94
88	2987	13 00 3.5	26 53 53	5911	32	16.1	14.43	12.52
89	2948	13 00 6.3	27 18 02	7858	32	18.5	16.87	14.99
91	3100	12 59 54.4	26 49 11	7994	36	12.1	16.98	15.34
94	3661	12 59 13.7	27 24 09	5644	33	15.5	15.77	13.84
95	2640	13 00 29.2	27 30 52	7395	38	14.1	16.33	15.02
96	2945	13 00 6.3	27 46 32	6175	32	19.7	16.27	14.33
97	2615	13 00 32.5	27 45 58	6662	32	19.3	16.99	15.10
98	2599	13 00 33.7	27 38 15	7498	33	12.2	15.97	14.72
99	2776	13 00 19.1	27 33 13	5862	32	17.3	16.19	14.27
100	2721	13 00 22.4	27 37 24	7592	33	14.1	17.57	15.69
101	2393	13 00 54.7	27 47 08	8282	69	3.1	16.22	14.31
102	2603	13 00 33.4	27 49 27	8176	33	13.5	17.48	15.69
103	2942	13 00 6.3	27 41 06	7561	32	17.8	16.64	14.82
105	2783	13 00 18.6	27 48 56	5328	36	8.4	17.59	15.66
106	2582	13 00 35.7	27 34 27	5064	36	8.9	16.24	14.39
107	2894	13 00 10.4	27 35 42	5587	32	14.4	17.26	15.36
108	2866	13 00 12.6	27 46 54	7008	33	14.2	16.97	15.22
110	2601	13 00 33.6	27 30 14	5602	32	15.2	16.88	15.60
111	2688	13 00 25.2	27 33 08	7258	33	13.6	17.80	15.96
115	4106	12 58 39.9	26 45 33	7467	31	19.3	17.01	15.76
117	4135	12 58 37.2	27 10 35	7705	32	13.8	15.81	14.33
120	3837	12 59 1.8	26 48 56	7117	33	17.0	14.60	12.59
123	4206	12 58 32.1	27 27 22	7007	32	17.8	16.48	14.58
124	4192	12 58 33.1	27 21 51	6950	32	18.1	16.34	14.41
126	4159	12 58 35.4	27 15 52	7380	32	15.9	16.15	14.77
127	4351	12 58 18.7	27 18 38	7447	31	18.4	17.04	15.39
130	4147	12 58 36.3	27 06 15	7954	31	22.0	15.41	13.49
131	4294	12 58 25.3	27 11 59	8035	38	7.2	17.90	16.04
132	4124	12 58 37.9	27 27 50	6243	43	5.4	16.67	14.72
133	3238	12 59 41.3	27 39 35	6742	32	18.8	16.88	14.95
134	3298	12 59 37.8	27 46 36	6766	34	11.2	17.50	15.75
135	3296	12 59 37.9	27 54 26	8005	33	17.4	16.08	14.14
136	3165	12 59 47.1	27 42 38	8324	31	21.5	14.91	13.02

TABLE 1—*Continued*

Fiber No. (1)	GMP83 Number (2)	R.A.[a] (3)	Decl.[a] (4)	cz (km s^{-1}) (5)	δ cz (km s^{-1}) (6)	R (7)	b (8)	r (9)
137	3400	12 59 30.8	27 53 03	4692	35	12.2	15.55	13.63
138	3271	12 59 39.8	27 34 36	5012	32	13.4	16.63	15.23
139	3178	12 59 46.1	27 51 26	8096	31	23.8	16.27	14.45
140	3071	12 59 56.2	27 44 47	8883	50	8.2	17.39	16.07
141	3092	12 59 54.9	27 47 45	8250	32	16.6	17.66	15.81
142	3423	12 59 29.4	27 51 00	6797	34	16.4	15.95	14.07
143	3201	12 59 44.4	27 54 45	6679	32	19.6	15.70	13.79
144	3510	12 59 23.2	27 54 45	6821	36	11.5	14.46	12.59
145	3557	12 59 20.2	27 53 09	6468	32	17.9	16.53	14.70
146	3012	13 00 1.5	27 43 51	8051	41	7.4	17.52	15.74
147	3493	12 59 24.9	27 44 19	6027	32	17.5	16.55	14.68
148	3313	12 59 37.0	27 49 32	6244	32	15.7	17.64	15.83
149	3403	12 59 30.7	27 47 29	7762	31	20.3	17.06	15.23
150	3262	12 59 39.9	27 51 17	3747	40	6.9	16.77	14.94
151	3339	12 59 35.3	27 51 49	6274	32	14.9	17.81	15.91
152	3126	12 59 51.0	27 49 58	7921	33	14.1	17.69	15.74
153	3730	12 59 8.2	27 47 02	7033	33	18.0	15.37	13.40
155	3588	12 59 18.5	27 30 48	6009	37	8.2	18.01	16.31
156	3829	12 59 1.6	27 32 13	8570	42	6.9	17.73	15.80
158	3739	12 59 7.4	27 46 06	6336	33	14.9	15.80	13.94
160	3958	12 58 52.1	27 47 05	5662	33	15.8	15.96	14.14
161	3660	12 59 13.5	27 46 28	6818	31	20.8	15.85	13.91
162	3697	12 59 10.3	27 37 11	5725	32	17.2	16.67	14.80
163	3879	12 58 58.1	27 35 41	5998	32	18.7	16.39	14.52
164	3997	12 58 48.7	27 48 37	5918	33	15.9	15.37	13.48
165	4017	12 58 47.4	27 40 29	8378	32	18.8	15.04	13.11
166	3782	12 59 4.6	27 54 39	6408	32	19.2	16.75	14.84
167	3943	12 58 53.0	27 48 48	5523	33	13.9	16.96	15.11
168	3779	12 59 5.3	27 38 39	5387	33	11.9	15.36	13.85
169	3733	12 59 8.0	27 51 18	6556	32	19.4	15.87	13.99
172	3896	12 58 56.1	27 50 00	7473	33	13.8	14.99	13.27
173	4522	12 58 1.5	27 29 22	7633	31	20.3	15.78	13.92
174	4502	12 58 3.5	27 40 56	7220	32	16.7	18.02	16.10
175	4447	12 58 9.7	27 32 57	6970	33	15.0	17.83	15.89
178	4579	12 57 56.3	27 34 52	4984	31	21.6	16.94	15.81
179	4209	12 58 31.6	27 40 24	6910	32	18.3	17.01	15.13
180	4255	12 58 28.4	27 33 33	7554	36	11.6	16.63	14.94
181	4469	12 58 6.8	27 34 36	7504	36	9.0	17.85	15.91
182	4156	12 58 35.2	27 35 47	7694	35	13.8	14.71	12.96
183	4060	12 58 42.6	27 45 37	8662	66	5.7	17.79	16.48
184	4348	12 58 18.2	27 50 54	7612	45	8.8	18.04	16.69
185	4117	12 58 38.4	27 32 38	5964	32	17.1	16.77	14.90
187	4083	12 58 40.8	27 49 37	6163	37	8.2	17.81	15.98
190	4341	12 58 19.2	27 45 43	5420	32	15.1	17.32	15.52
191	4499	12 58 3.5	27 48 53	7118	32	20.4	16.18	14.33
192	4314	12 58 22.0	27 53 32	7276	32	16.0	17.76	15.89
193	4731	12 57 43.0	26 51 08	6356	31	20.3	15.85	13.99
194	4793	12 57 36.5	27 01 52	7328	32	19.6	16.27	14.28
196	4582	12 57 56.7	27 02 14	7419	33	13.3	16.70	14.83
197	4518	12 58 3.2	26 54 57	8188	32	18.0	15.98	14.11
201	4463	12 58 9.2	26 39 51	7314	31	17.0	17.34	15.78
202	4912	12 57 26.7	26 41 37	7248	34	11.0	17.70	15.77
204	4692	12 57 45.7	27 25 45	8334	34	13.0	17.56	15.73
205	4479	12 58 6.1	27 25 08	5759	34	11.3	17.62	15.76
209	4918	12 57 25.3	27 24 16	4863	31	21.3	16.31	14.37
210	4535	12 58 0.8	27 27 14	7662	32	16.4	17.95	16.04
212	4961	12 57 21.5	27 01 22	8009	33	14.6	17.80	16.00
213	4928	12 57 23.9	27 29 46	7329	41	8.5	15.43	13.40
216	4714	12 57 43.2	27 34 39	7204	33	14.2	17.71	15.87
218	4829	12 57 32.8	27 36 37	6052	34	14.5	14.92	12.97
219	4794	12 57 35.8	27 29 35	7299	32	20.1	15.41	13.42
220	4907	12 57 25.8	27 32 46	5580	33	16.0	16.09	14.21
221	5051	12 57 9.4	27 27 59	7447	32	19.4	15.55	13.60
222	4597	12 57 54.4	27 29 26	4962	34	10.8	16.47	14.62
223	4933	12 57 23.5	27 45 58	9115	32	19.0	16.39	14.43
224	4653	12 57 48.1	27 52 58	5849	32	19.0	15.72	13.88
225	4664	12 57 47.3	27 49 59	6041	32	19.1	16.25	14.39
226	5100	12 57 4.2	27 43 48	8884	36	9.9	17.34	15.63
227	4945	12 57 21.7	27 52 49	7427	32	18.7	16.72	15.00

TABLE 1—*Continued*

Fiber No. (1)	GMP83 Number (2)	R.A.[a] (3)	Decl.[a] (4)	cz (km s^{-1}) (5)	δ cz (km s^{-1}) (6)	R (7)	b (8)	r (9)
228	4679	12 57 46.2	27 45 25	6133	32	18.0	16.11	14.17
229	4987	12 57 16.8	27 37 06	7238	32	18.7	16.86	14.97
231	4974	12 57 17.8	27 48 39	7136	33	15.7	16.59	14.98
232	5096	12 57 4.6	27 46 22	7577	36	9.0	17.00	15.17
234	5290	12 56 43.2	26 44 30	6950	33	15.2	17.44	15.56
236	5365	12 56 34.6	27 13 38	7197	39	8.5	16.60	14.87
237	5136	12 57 1.7	27 22 19	6979	32	19.9	16.66	14.70
238	5514	12 56 20.5	26 42 14	6558	33	15.0	17.39	15.54
240	5395	12 56 32.0	27 03 19	6105	32	18.5	16.19	14.33
241	5226	12 56 51.2	26 53 56	6247	32	19.9	15.42	13.68
242	5424	12 56 29.1	26 57 25	7035	32	19.8	15.20	13.32
243	5526	12 56 16.7	27 26 45	6386	31	20.6	16.50	14.56
244	5422	12 56 28.5	27 17 29	7526	33	10.7	15.74	14.18
246	5234	12 56 49.7	27 05 37	6934	33	14.3	15.89	13.87
247	5250	12 56 47.8	27 25 15	7758	32	17.2	17.12	15.29
248	5279	12 56 43.5	27 10 43	7607	33	18.4	14.00	11.98
249	5283	12 56 43.5	27 02 04	5586	32	18.1	16.88	15.03
250	5038	12 57 10.8	27 24 17	6193	33	13.0	16.25	14.33
251	5254	12 56 47.4	27 17 32	7854	36	9.4	17.86	16.15
252	5032	12 57 12.0	27 06 11	7333	34	11.2	17.66	15.78
253	5102	12 57 4.3	27 31 33	8296	33	13.0	17.66	15.70
254	5495	12 56 19.8	27 45 03	6859	32	19.7	15.80	13.87
255	5912	12 55 35.7	27 46 01	6680	33	14.4	17.17	15.29
256	5546	12 56 14.6	27 30 22	7422	32	18.3	17.51	15.60
257	5850	12 55 44.3	27 42 59	7138	32	14.7	18.03	16.06
258	5599	12 56 9.9	27 50 39	7566	31	21.9	15.96	13.95
259	5643	12 56 6.1	27 40 40	4909	31	21.3	16.00	14.51
260	5362	12 56 34.2	27 41 14	6872	32	17.4	17.83	15.93
261	5428	12 56 26.6	27 49 50	6268	32	20.4	15.69	13.80
262	5434	12 56 26.3	27 43 38	6823	31	21.2	16.96	15.03
264	5926	12 55 34.1	27 50 30	6997	31	20.6	16.94	15.00
266	5568	12 56 13.4	27 45 00	6817	91	2.9	15.19	13.66
267	5721	12 55 57.5	27 54 17	6551	32	14.9	17.44	15.48
268	5364	12 56 34.2	27 32 20	7086	32	20.1	16.03	14.07
271	5641	12 56 6.5	27 38 52	7593	32	19.9	16.74	14.88
272	5799	12 55 49.0	27 54 21	6930	31	21.4	16.49	14.57
273	6545	12 54 16.0	27 18 13	6422	32	20.1	15.32	13.32
275	6617	12 54 5.5	27 04 07	7589	32	18.9	15.41	13.46
279	6409	12 54 36.8	26 56 05	5913	32	16.5	15.59	13.75
280	5704	12 56 1.7	26 45 23	5722	33	15.3	16.57	14.67
282	6703	12 53 45.5	27 14 58	6902	35	11.4	17.73	15.88
285	6690	12 53 46.6	27 23 09	8317	43	5.0	17.84	15.92
287	6503	12 54 22.2	27 05 02	8427	32	21.1	16.51	14.52
289	5886	12 55 41.3	27 15 02	7105	33	17.8	15.05	13.06
291	5676	12 56 4.0	27 09 01	7337	33	15.8	17.97	16.05
292	6474	12 54 24.7	27 21 50	7833	39	8.6	17.55	15.64
293	6219	12 55 0.8	27 29 00	6968	36	7.9	17.34	15.51
294	6421	12 54 33.2	27 37 58	7265	33	13.8	15.96	13.91
295	6043	12 55 20.0	27 51 59	6978	32	16.3	16.33	14.46
296	5975	12 55 29.1	27 31 17	6983	32	21.5	14.36	12.49
297	6390	12 54 37.4	27 41 31	8453	32	19.1	17.66	15.79
302	...	12 53 37.9	27 47 03	5088	32	18.2	15.80	13.89
303	5999	12 55 25.0	27 47 53	7382	32	19.7	15.20	12.93
304	6109	12 55 13.9	27 42 32	6647	32	15.1	17.70	15.76
306	...	12 53 30.3	27 40 30	5919	31	20.8	17.50	15.59
307	5960	12 55 30.6	27 32 39	7024	32	14.8	16.76	14.80
308	6701	12 53 44.1	27 46 51	6640	32	16.5	17.81	15.96
309	6479	12 54 22.7	27 44 40	7102	36	9.5	18.04	16.27
311	...	12 53 35.5	27 45 31	7463	33	14.4	16.95	15.08
312	5978	12 55 27.8	27 39 22	6997	32	18.8	15.33	13.36

NOTE.—Units of right ascension are hours, minutes, and seconds, and units of declination are degrees, arcminutes, and arcseconds (J2000.0).

[a] Position of the fiber. For some objects this is a bit off of the galaxy.

(running from 1 to 320), while column (2) is the GMP83 number when appropriate (three of our galaxies do not have a corresponding GMP83 detection). Columns (3) and (4) give the right ascension and declination of the fiber center (not necessarily the galaxy centroid). In column (5) we present the cross-correlation redshift corrected to the heliocentric reference frame. The redshift error, in column (6), includes the error in the wavelength calibration com-

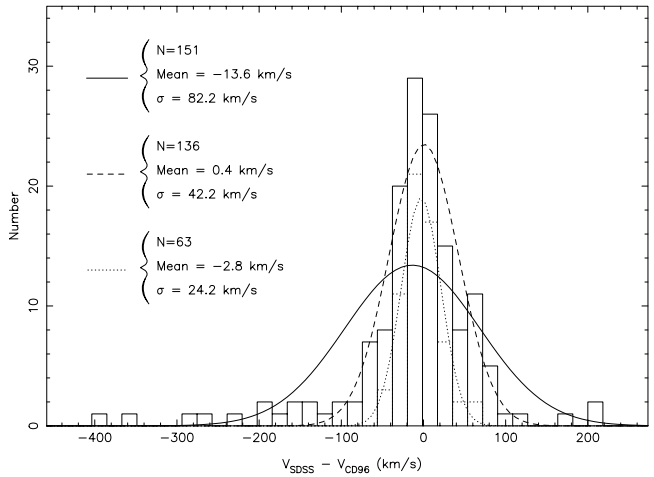


FIG. 6.—Distribution of the difference in *cz* between the our redshift measurements (Table 1) and those in the literature. The solid histogram represents all 151 matches. The solid line is a Gaussian fit to the whole histogram. The dashed line is a Gaussian fit to the histogram with 3 σ clipping rejection. The dotted histogram counts only the galaxies that were measured by CD96 and not taken from the literature by these authors. The dotted histogram is a Gaussian fit to it. (See text for further details.)

bined in quadrature with the error resulting from the cross-correlation technique. The usual R cross-correlation coefficient is listed in column (7). In most cases, we simply chose the cross-correlation redshift with the largest R value out of the 34 possible template cross-correlation redshifts. There were a few cases where the best R was in clear disagreement with our visual redshift measurements; in these cases we reinspected the spectrum and quote, as our final redshift, the template with the highest R coefficient consistent with our visual redshift. These rare cases were typically due to noncorrected cosmic rays or sky residuals that produced a confident cross-correlation with one of the emission-line templates. Finally, in columns (8) and (9), we provide the magnitudes for the galaxy taken from the SuperCOSMOS catalog and calibrated to the GMP83 system.

We have compared our redshift measurements with the data available in the literature. We have matched our catalog with the redshift compilation of CD96, as well as data from the NED[26] database. We found 151 galaxies that match previous known redshifts. The remaining 45 galaxies, approximately a quarter of our Coma redshifts, represent new measurements. In Figure 6, we show the comparison between our redshift measurements and those in the literature. The solid histogram represents the 151 matches, where 148 come from the compilation of CD96 (including their own measurements and values in the literature), and the other three are taken from NED. The solid histogram is a Gaussian fit to the entire distribution. The fit is poor because of the extended tails. We can improve the fit considerably if we reject 3 σ outliers (15 galaxies; see Fig. 6). We attribute these outliers to the heterogeneity of the data where different data sets from the literature have different calibration errors. Also, these discrepancies could be in part attributed to the internal dynamics of the observed galaxies because of the different fiber and/or slit placements. We can improve the fit even further by restricting ourselves to the largest homogeneous data set from the literature i.e., the 63 new redshift measurements of CD96. We then find excellent agreement between our measurements (the dotted histogram and Gaussian fit) with a mean offset of 3 km s^{-1} and an rms scatter of 24 km s^{-1}. Overall, the agreement of our redshift determinations with the literature is remarkably good. The RMS scatter between data sets indicates that our estimate of the errors in the wavelength calibration is accurate.

7. SPECTRAL CLASSIFICATIONS

In this section, we consider the spectral classification of our Coma galaxies. We have investigated four different algorithms, all of which could be implemented for the main SDSS galaxy survey. The first algorithm is based on visual inspections of the spectra but quantified using measurements of the equivalent widths[27] of the lines seen in the spectrum. The next two algorithms, wavelets and principal component analysis (PCA), were used to objectively classify the spectra using the visual inspections to define relevant thresholds in wavelet and eigenspace. The final classification scheme attempts to define a physical classification scheme based on synthetic models of galaxies.

7.1. *Line-Strength Classifications*

We started by visually classifying the spectra into five classes which could then be compared with the other algorithms. We first divide the spectra into two broad classes: emission and absorption-line galaxies. Absorption-line spectra were then subdivided into normal absorption-line systems, and objects with strong Balmer lines or poststarburst galaxies. The spectra showing emission lines were subdivided into three categories depending on the strength of the emission lines.

For our visual and line-strength classification scheme, we were able to use both the blue side of the spectrum and the presence of Hα in the red end of the spectrum. Unfortunately the other classification algorithms could not use the red side of the spectrum due to the condensation problems discussed above. Since Hα is a powerful indicator of star formation, we believe that one of the classification schemes should utilize these data even if the others could not. Moreover, the other algorithms used our line-strength classifications to quantify star formation in Coma and therefore, it was justified to make the line-strength classification as strong as possible by using all data available.

Using our equivalent width measurements, we divided the spectra in the five following types: (1) absorption-line galaxies (AB), which have spectra without Hα in emission and with the sum of the equivalent widths of Hδ, Hγ and Hβ smaller than 15 Å; (2) poststarburst galaxies (PS), which have no Hα in emission, $W_o(\mathrm{H}\alpha) > 0$, and $W_o(\mathrm{H}\delta + \mathrm{H}\gamma + \mathrm{H}\beta) > 15$ Å; (3) absorption-line–dominated galaxies, but with Hα in emission and modest Hβ emission (AB + EM), $W_o(\mathrm{H}\alpha) < 0$ and $W_o(\mathrm{H}\beta) > -5$ Å; (4) emission- and absorption-line galaxies (EM + AB), which we define using $W_o(\mathrm{H}\alpha) < 0$ and $-5 < W_o(\mathrm{H}\beta) < -15$ Å; (5) emission-line–

[26] NED is the NASA/IPAC Extragalactic Database, operated by the Jet Propulsion Laboratory, Caltech, under contract with NASA.

[27] All equivalent widths given in this paper are rest-frame equivalent widths $W_o = W_{\mathrm{observed}}/(1 + z)$ and follow the following convention unless otherwise stated: absorption-line equivalent widths are positive and emission-line equivalent widths are negative.

dominated spectra (EM), which have $W_o(\mathrm{H}\alpha) < 0$ and $W_o(\mathrm{H}\beta) < -15$ Å. We present these classifications in Table 2 where column (1) is the same extraction number as given Table 1, column (2) is the classification based on the line-strength criteria given above, column (3) is the PCA classification and column (4) is the wavelet classification (see below). The results of the synthetic model fitting and the parameters of the PCA classification, both of which are discussed below, are listed in columns (5) through (10) and columns (11) through (16), respectively.

In Figure 3 we show the distribution on the sky of the 196 galaxies given in Tables 1 and 2. The half-circle shape observed on the data is due to the availability of only one spectrograph. The presence of the NGC 4839 group is obvious in the southwest region of the cluster. The plotting symbols reflect the five different galaxy types defined above.

7.2. *Principal Component Analysis*

To quantify the visual classification discussed above, we have implemented a principal component analysis (PCA) of our Coma spectra (Mittaz, Penston, & Snijders 1990; Connolly et al. 1995). The basis of this method consists of describing a multidimensional distribution of variables with a minimum number of dimensions. In our case, we are searching for the minimum number of eigenspectra needed to describe the whole spectral data set. We can thereafter classify each spectrum as a function of these eigenspectra. We have used here a version of the official SDSS spectroscopic reduction software which already implements the PCA analysis of Connolly et al. (1995).

7.2.1. *Data Preparation*

As mentioned above, only the blue spectra were used for the PCA analysis. To prepare the spectra, we first interpolated over the [O I] λ5577 and NaD $\lambda\lambda$5890, 5896 doublet sky emission lines since many of the spectra contained significant residuals of these strong skylines. Next, each spectrum was blueshifted to the galaxy's rest frame and rebinned to the wavelength range 3750→5900 Å at a dispersion of 1.125 Å pixel^{-1}. Then we subtracted the continuum from the spectra using a fourth order polynomial. We have also carried out the PCA analysis without continuum subtraction, but we obtain better discriminating power to reproduce the line-strength classification employing the continuum-subtracted sample. Finally, we smoothed each spectrum with a Gaussian with a width set by the spectrograph resolution of $R = 1800$ which produced a set of 673 pixel spectra, binned over a common wavelength range, which could then be used as input to the PCA algorithm.

7.2.2. *Eigenspectra Derivation*

Using these prepared spectra, we performed the PCA methodology presented in Connolly et al. (1995) and Connolly & Szalay (1999). We present a very brief summary below, but for a more detailed description see Connolly et al. (1995). We regard each spectrum as a vector, f_λ, where λ is an index running on wavelength. We represent the whole spectra set by a matrix $f_{\lambda,i}$, where the index i runs through the individual spectra. We apply a uniform normalization to each spectrum, so that the weighted sum of the squared flux is unity. Thus, our normalized spectra are computed as

$$F_{\lambda,i} = \frac{f_{\lambda,i}}{\sqrt{\sum_\lambda f_{\lambda,i}^2 W_\lambda}} . \tag{1}$$

In all cases a uniform weight was applied, so that $W_\lambda = 1$ for all wavelengths λ. We want to construct an orthogonal basis for the space spanned by the spectra, which we call eigenspectra. We derive these eigenspectra by diagonalizing the correlation matrix C_{ij}, given by

$$C_{ij} = \sum_\lambda F_{\lambda,i} F_{\lambda,j} W_\lambda . \tag{2}$$

By diagonalizing the correlation matrix, we find the matrix R that produces the diagonal matrix Λ whose components are the eigenvalues, γ_i, of the orthogonal eigenspectra, $e_{\lambda,i}$,

$$R^\dagger C R = \Lambda , \tag{3}$$

$$R^\dagger_{i,j}(\sum_\lambda F_{\lambda,i} F_{\lambda,j}) R_{i,j} = \Lambda_{i,j} ,$$

$$R^\dagger_{i,j} F_{\lambda,j} F_{\lambda,j} R_{i,j} = e_{\lambda,i} e^\dagger_{\lambda,j} = \gamma_i \delta_{i,j} ,$$

$$\Rightarrow R^\dagger_{i,j} F_{\lambda,j} = e_{\lambda,i} . \tag{4}$$

In Figure 7, we show the distribution of the first 20 eigenvalues. The two curves are the percentage contribution (compared with a fully reconstructed spectrum using all eigenvalues) of the N^{th} eigenvalue (decreasing curve on a log scale) and the percentage contribution of all the eigenvalues less than or equal to N (the increasing curve on a linear scale). As one can see the relative contribution of each eigenspectrum falls off rapidly; it is possible to account for $\sim$90% of the variance in our sample using a reasonably small number of eigenspectra ($\leq$10). The remaining $\sim$10% of the variance is probably mostly noise in the data, but may also partly be due to complex, real variations in the galaxy spectra. Following the methodology of Connolly et al. (1995), we limit our classification to the first three components, as these eigenspectra contain virtually all the usable information from a classification standpoint, as we will illustrate below. In our analysis, these three components account for 87% of the variance in our sample. By contrast, the first two to three components for eigensystems derived from synthetic spectra (e.g., Connolly & Szalay 1999; Ronen et al. 1999) generally account for 98%–99% of the variance, while the preliminary eigensystem derived for the 2dF Galaxy Redshift Survey (Folkes et al. 1999) contained about 66% of the total variance within the first three

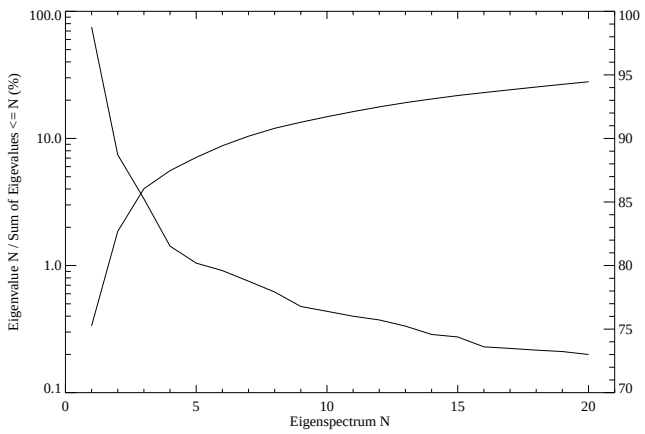


FIG. 7.—Distribution of the first 20 eigenvalues. The decreasing function is the percentage contribution of the N^{th} eigenvalue, and uses the left logarithmic axis. The increasing function is the cumulative percentage contribution by the first N eigenvalues, and uses the right linear axis.

TABLE 2

GALAXY CLASSIFICATIONS

				SPECTRAL_1			SPECTRAL_2			PRINCIPAL COMPONENT ANALYSIS COEFFICIENTS					
FIBER NO. (1)	LINE STRENGTHS (2)	PCA (3)	WAVELET (4)	Age (Gyr) (5)	SF (6)	χ^2/ν (7)	Age (Gyr) (8)	τ (Gyr) (9)	χ^2/ν (10)	c_1 (11)	c_2 (12)	c_3 (13)	θ(14)	ϕ (15)	Radius^2 (16)
3	AB	AB	AB	5.00	1	0.78	4.41	0.009	0.78	0.781	−0.069	0.128	9.30	−5.03	0.632
4	AB	AB	AB	6.14	2	0.51	4.20	0.607	0.51	0.846	−0.071	0.109	7.33	−4.80	0.733
10	AB	AB	AB	17.00	3	0.55	12.81	2.117	0.58	0.970	−0.112	−0.023	−1.35	−6.58	0.954
11	AB	AB	AB	13.79	1	2.68	18.86	2.718	2.45	0.948	−0.181	−0.178	−10.48	−10.79	0.962
12	EM+AB	EM	EM	2.26	3	0.79	1.21	0.368	0.93	0.335	0.843	−0.219	−13.53	68.31	0.871
13	AB	AB+EM	AB	1.98	1	0.91	1.20	0.002	0.90	0.534	0.243	0.239	22.16	24.52	0.401
14	AB	AB	AB	18.76	5	0.61	7.53	1.284	0.71	0.974	−0.044	0.046	2.72	−2.60	0.953
21	AB	AB	AB	17.04	2	2.52	16.63	2.718	2.62	0.957	−0.127	−0.040	−2.39	−7.55	0.935
27	AB	AB	AB	19.00	4	0.96	12.27	2.117	1.06	0.979	−0.022	0.062	3.64	−1.26	0.962
28	AB	AB	AB	19.00	4	0.47	12.35	2.117	0.52	0.946	0.079	0.175	10.47	4.77	0.931
29	AB	AB	AB	17.79	4	0.44	11.76	2.117	0.50	0.915	0.008	0.072	4.51	0.52	0.843
30	AB	AB	AB	16.26	5	0.17	3.43	0.472	0.18	0.662	0.200	0.286	22.49	16.82	0.561
31	EM+AB	EM	EM	3.04	3	7.99	1.25	0.287	8.81	0.478	0.796	−0.097	−5.97	59.01	0.872
32	AB	AB	AB	19.00	4	0.74	12.58	2.117	0.82	0.988	−0.041	0.025	1.44	−2.40	0.979
34	AB+EM	AB+EM	EM	17.88	5	2.28	19.00	4.482	2.69	0.786	0.288	−0.259	−17.16	20.12	0.768
40	AB	AB	AB	16.98	5	0.42	3.50	0.472	0.48	0.758	−0.023	0.091	6.87	−1.75	0.584
43	AB	AB	AB	17.16	4	0.62	11.48	2.117	0.72	0.958	0.023	0.145	8.60	1.36	0.939
45	PS	PS	PS	1.26	1	0.37	0.60	0.018	0.39	0.483	0.484	0.587	40.61	45.06	0.813
50	AB	AB	AB	19.00	2	2.47	18.18	2.718	2.36	0.987	−0.116	−0.008	−0.47	−6.73	0.988
55	AB	AB	AB	13.46	2	0.89	11.02	1.649	0.94	0.984	−0.067	0.005	0.31	−3.91	0.973
58	PS	PS	PS	1.46	2	4.11	1.12	0.174	3.69	0.696	0.518	0.374	23.32	36.69	0.892
61	AB	AB	AB	19.00	5	0.65	13.58	2.718	0.78	0.929	0.087	0.195	11.78	5.37	0.908
65	AB	AB	AB	19.00	4	1.10	12.59	2.117	1.21	0.978	−0.036	0.068	3.96	−2.11	0.962
66	AB	AB	AB	18.61	4	0.85	9.97	1.649	0.96	0.984	−0.046	0.062	3.59	−2.65	0.974
68	AB	AB	AB	9.82	2	0.60	6.93	1.000	0.62	0.976	0.024	0.087	5.10	1.41	0.960
69	AB	AB	AB	18.27	2	2.63	14.62	2.117	2.66	0.971	−0.134	−0.083	−4.83	−7.86	0.968
70	AB	AB	AB	14.57	2	1.67	11.46	1.649	1.70	0.978	−0.117	−0.017	−1.00	−6.82	0.971
74	AB	AB	AB	19.00	1	3.75	19.00	0.011	3.73	0.841	−0.100	0.015	1.01	−6.76	0.717
75	AB	AB	AB	18.00	1	15.71	19.00	0.002	15.19	0.954	−0.122	−0.056	−3.34	−7.29	0.928
76	AB	AB	AB	13.00	1	3.19	14.60	1.649	3.18	0.844	−0.008	0.177	11.87	−0.56	0.743
84	EM+AB	EM	AB	3.98	4	0.29	2.09	0.607	0.36	0.388	0.788	−0.240	−15.26	63.79	0.829
85	AB+EM	AB+EM	AB	18.41	2	2.65	19.00	3.490	2.67	0.805	0.409	−0.060	−3.78	26.92	0.819
86	AB	AB	AB	19.00	3	0.98	16.14	2.718	1.05	0.981	−0.066	0.035	2.06	−3.84	0.967
87	AB	AB	AB	17.07	1	0.48	19.00	2.117	0.47	0.934	−0.058	0.049	3.02	−3.57	0.878
88	AB	AB	AB	13.83	1	2.25	18.94	2.718	2.10	0.971	−0.143	−0.089	−5.20	−8.40	0.972
89	AB	AB	AB	17.58	2	0.70	14.46	2.117	0.73	0.967	0.004	0.128	7.54	0.22	0.952
91	AB+EM	PS	PS	1.98	1	1.23	1.20	0.002	1.20	0.755	0.463	0.420	25.39	31.52	0.961
94	AB	AB	AB	17.53	1	2.41	16.74	0.011	2.33	0.950	−0.204	−0.165	−9.64	−12.14	0.970
95	PS	PS	PS	1.39	1	1.79	0.89	0.105	1.92	0.544	0.528	0.564	36.65	44.12	0.893
96	AB	AB	AB	16.00	1	1.12	18.37	2.117	1.08	0.969	−0.166	−0.121	−7.02	−9.73	0.981
97	AB	AB	AB	19.00	2	0.83	17.57	2.718	0.86	0.983	−0.109	−0.053	−3.05	−6.35	0.982
98	EM+AB	EM	EM	1.96	3	4.15	0.86	0.223	4.62	0.328	0.851	−0.178	−11.06	68.94	0.864
99	AB	AB	AB	15.49	1	1.50	17.97	2.117	1.44	0.962	−0.187	−0.131	−7.59	−10.99	0.977
100	AB	AB	AB	18.22	2	0.52	17.21	2.718	0.53	0.962	0.029	0.071	4.20	1.70	0.931

TABLE 2—*Continued*

				Spectral_1			Spectral_2			Principal Component Analysis Coefficients					
Fiber No. (1)	Line Strengths (2)	PCA (3)	Wavelet (4)	Age (Gyr) (5)	SF (6)	χ^2/ν (7)	Age (Gyr) (8)	τ (Gyr) (9)	χ^2/ν (10)	c_1 (11)	c_2 (12)	c_3 (13)	θ(14)	ϕ (15)	Radius^2 (16)
101	AB	AB+EM	AB	19.00	1	0.20	19.00	0.002	0.19	0.435	0.164	0.192	22.41	20.69	0.253
102	AB	AB	PS	15.67	4	0.63	3.89	0.472	0.66	0.909	0.169	0.292	17.52	10.56	0.941
103	AB	AB	AB	16.17	2	1.03	13.88	2.117	1.08	0.982	−0.078	−0.032	−1.86	−4.56	0.971
105	AB	AB	AB	17.35	3	0.69	15.44	2.718	0.73	0.902	−0.107	−0.068	−4.30	−6.79	0.830
106	AB+EM	AB+EM	AB	18.09	5	2.06	13.15	2.718	2.52	0.791	0.342	0.009	0.62	23.40	0.743
107	AB	AB	AB	16.50	2	0.87	16.51	2.718	0.89	0.937	−0.071	−0.043	−2.61	−4.31	0.886
108	AB	AB	AB	14.27	4	1.12	4.11	0.607	1.15	0.964	−0.029	−0.004	−0.24	−1.73	0.930
110	EM+AB	EM	EM	2.56	3	2.54	1.13	0.287	2.83	0.260	0.751	−0.465	−30.31	70.92	0.848
111	AB	AB	AB	17.33	2	0.50	16.82	2.718	0.51	0.934	−0.002	0.034	2.07	−0.14	0.874
115	EM	EM	EM	0.02	5	6.54	0.06	90.017	6.04	−0.086	0.534	−0.529	−44.34	80.80	0.572
117	EM+AB	EM	EM	4.62	4	3.05	1.58	0.368	3.60	0.449	0.849	−0.093	−5.54	62.11	0.932
120	AB	AB	AB	17.58	1	4.64	19.00	2.117	4.47	0.947	−0.160	−0.145	−8.57	−9.59	0.942
123	AB	AB	AB	10.33	2	1.47	5.94	0.779	1.56	0.977	−0.143	−0.062	−3.59	−8.33	0.978
124	AB	AB	AB	4.01	1	0.96	3.46	0.105	0.95	0.979	−0.069	0.022	1.31	−4.01	0.964
126	EM	EM	EM	2.57	6	5.02	1.18	0.472	6.09	0.146	0.810	−0.467	−29.58	79.78	0.895
127	EM	EM	EM	12.66	7	2.13	17.58	9.488	1.95	0.142	0.778	−0.552	−34.91	79.63	0.930
130	AB	AB	AB	13.61	2	1.45	11.06	1.649	1.45	0.985	−0.080	0.019	1.09	−4.62	0.976
131	AB+EM	AB+EM	PS	11.54	5	0.54	2.75	0.472	0.60	0.739	0.459	0.144	9.36	31.83	0.778
132	AB+EM	AB+EM	AB	15.82	6	0.67	2.37	0.368	0.74	0.645	0.268	−0.080	−6.52	22.56	0.494
133	AB	AB	AB	19.00	3	0.54	16.03	2.718	0.56	0.965	−0.067	−0.031	−1.80	−3.97	0.938
134	AB	AB	AB	13.68	2	0.33	11.21	1.649	0.33	0.915	−0.015	0.025	1.55	−0.92	0.837
135	AB	AB	AB	18.21	2	2.06	14.62	2.117	2.12	0.969	−0.110	−0.061	−3.58	−6.48	0.955
136	AB	AB	AB	14.25	1	1.87	19.00	2.718	1.77	0.970	−0.101	0.015	0.87	−5.95	0.951
137	AB	AB	AB	17.83	2	3.63	14.50	2.117	3.68	0.935	−0.173	−0.163	−9.75	−10.46	0.932
138	EM+AB	EM	AB	0.97	2	2.10	0.94	0.223	2.30	0.437	0.782	−0.146	−9.26	60.78	0.824
139	AB	AB	AB	18.83	2	1.75	14.95	2.117	1.71	0.978	−0.111	0.013	0.76	−6.45	0.970
140	AB+EM	PS	PS	1.22	1	1.22	0.76	0.135	1.24	0.511	0.570	0.492	32.75	48.10	0.828
141	AB+EM	AB	AB	18.80	3	0.73	15.82	2.718	0.75	0.964	0.019	0.059	3.51	1.13	0.932
142	AB	AB	AB	15.10	1	2.88	17.74	2.117	2.75	0.945	−0.179	−0.180	−10.59	−10.72	0.958
143	AB	AB	AB	16.00	2	2.19	13.82	2.117	2.27	0.986	−0.108	−0.072	−4.14	−6.24	0.989
144	AB	AB	AB	19.00	1	0.46	18.95	0.050	0.45	0.932	−0.121	−0.105	−6.35	−7.39	0.893
145	AB	AB	AB	13.52	2	0.98	11.10	1.649	0.99	0.979	−0.094	−0.005	−0.29	−5.51	0.967
146	AB	AB	AB	19.00	5	0.37	6.48	1.000	0.40	0.820	0.157	0.209	14.07	10.82	0.740
147	AB	AB	AB	12.31	1	1.71	15.80	2.117	1.64	0.960	−0.187	−0.160	−9.29	−11.01	0.983
148	AB	AB	AB	14.14	2	1.03	11.34	1.649	1.05	0.965	−0.111	−0.054	−3.17	−6.58	0.947
149	AB	AB	AB	14.14	2	1.12	11.31	1.649	1.12	0.984	−0.026	0.032	1.84	−1.52	0.971
150	AB	AB	AB	19.00	1	0.86	19.00	0.002	0.82	0.695	−0.125	−0.042	−3.44	−10.21	0.500
151	AB	AB	AB	8.80	1	0.52	8.66	0.607	0.52	0.951	−0.095	−0.022	−1.32	−5.69	0.914
152	AB	AB	AB	14.02	1	0.59	16.92	2.117	0.58	0.962	0.019	0.061	3.62	1.15	0.930
153	AB	AB	AB	14.09	1	3.07	19.00	2.718	2.87	0.957	−0.159	−0.143	−8.37	−9.45	0.962
155	AB	AB	AB	15.35	4	0.29	4.42	0.607	0.31	0.808	−0.021	0.091	6.46	−1.46	0.661
156	AB	AB	AB	17.50	5	0.57	5.90	1.000	0.62	0.851	0.054	0.161	10.67	3.66	0.753
158	AB	AB	AB	19.00	2	0.51	18.16	2.718	0.50	0.960	−0.132	−0.113	−6.63	−7.80	0.951
160	AB	AB	AB	16.05	2	1.99	11.95	1.649	1.98	0.952	−0.184	−0.150	−8.79	−10.96	0.964

TABLE 2—*Continued*

				Spectral_1			Spectral_2			Principal Component Analysis Coefficients					
Fiber No. (1)	Line Strengths (2)	PCA (3)	Wavelet (4)	Age (Gyr) (5)	SF (6)	χ^2/ν (7)	Age (Gyr) (8)	τ (Gyr) (9)	χ^2/ν (10)	c_1 (11)	c_2 (12)	c_3 (13)	θ(14)	ϕ (15)	Radius[2] (16)
161	AB	AB	AB	16.49	2	1.54	13.97	2.117	1.59	0.984	−0.118	−0.070	−4.05	−6.82	0.987
162	AB	AB	AB	14.30	2	1.44	11.38	1.649	1.44	0.957	−0.173	−0.155	−9.05	−10.26	0.970
163	AB	AB	AB	17.89	2	1.71	14.53	2.117	1.69	0.963	−0.173	−0.159	−9.25	−10.19	0.982
164	AB	AB	AB	17.18	2	2.90	12.41	1.649	2.83	0.961	−0.161	−0.160	−9.34	−9.51	0.976
165	AB	AB	AB	19.00	2	2.01	15.25	2.117	1.98	0.943	−0.156	−0.101	−6.06	−9.41	0.923
166	AB	AB	AB	13.89	2	1.02	11.22	1.649	1.02	0.982	−0.134	−0.089	−5.11	−7.78	0.990
167	AB	AB	AB	12.87	1	0.70	16.08	2.117	0.68	0.938	−0.147	−0.105	−6.28	−8.90	0.913
168	EM+AB	EM	EM	1.15	1	10.68	0.74	0.174	12.44	0.205	0.632	−0.356	−28.16	72.04	0.567
169	AB+EM	AB	AB	18.31	2	2.44	17.08	2.718	2.54	0.945	−0.173	−0.175	−10.33	−10.38	0.954
172	AB+EM	AB+EM	AB	17.24	5	1.78	5.81	1.000	2.34	0.965	0.199	0.123	7.10	11.65	0.986
173	AB	AB	AB	19.00	2	1.59	17.96	2.718	1.55	0.983	−0.092	−0.019	−1.10	−5.34	0.974
174	AB	AB	AB	17.48	2	0.68	14.49	2.117	0.68	0.961	−0.039	−0.004	−0.25	−2.33	0.926
175	AB	AB	AB	16.49	2	0.92	16.54	2.718	0.92	0.949	−0.012	−0.023	−1.41	−0.71	0.902
178	EM+AB	EM	EM	2.00	4	1.64	1.08	0.368	2.02	0.194	0.791	−0.472	−30.10	76.19	0.887
179	AB	AB	AB	14.41	2	1.60	13.25	2.117	1.63	0.980	−0.084	−0.071	−4.12	−4.89	0.972
180	AB+EM	AB+EM	PS	12.64	5	2.61	3.33	0.607	3.02	0.801	0.465	0.208	12.64	30.14	0.902
181	AB	AB	AB	17.33	4	0.55	11.57	2.117	0.61	0.872	0.119	0.066	4.28	7.77	0.779
182	AB+EM	AB+EM	PS	14.38	5	12.00	3.51	0.607	14.82	0.921	0.283	0.173	10.16	17.06	0.957
183	PS	PS	PS	1.01	2	0.67	0.77	0.135	0.69	0.378	0.462	0.536	41.90	50.70	0.644
184	PS	PS	PS	1.29	1	0.68	0.83	0.135	0.70	0.482	0.592	0.527	34.60	50.84	0.861
185	AB	AB	AB	15.20	2	1.57	13.58	2.117	1.56	0.962	−0.133	−0.107	−6.28	−7.89	0.956
187	AB	AB	AB	4.55	2	0.51	3.32	0.472	0.51	0.772	−0.024	−0.067	−4.98	−1.78	0.602
190	AB	AB	AB	5.06	2	0.79	3.40	0.472	0.77	0.938	−0.015	−0.019	−1.16	−0.93	0.880
191	AB	AB	AB	19.00	2	2.23	14.97	2.117	2.17	0.973	−0.127	−0.097	−5.63	−7.44	0.971
192	AB	AB	AB	13.14	2	0.69	12.86	2.117	0.71	0.946	0.036	0.013	0.81	2.21	0.897
193	AB	AB	AB	3.53	1	1.57	3.81	0.472	1.53	0.981	−0.070	−0.001	−0.08	−4.07	0.967
194	AB	AB	AB	18.06	2	1.90	16.94	2.718	1.96	0.975	−0.103	−0.093	−5.44	−6.02	0.969
196	AB+EM	AB+EM	AB	15.53	5	1.92	4.46	0.779	2.56	0.949	0.161	0.061	3.63	9.60	0.930
197	AB	AB	AB	14.26	2	3.11	11.34	1.649	3.11	0.960	−0.084	0.031	1.82	−5.02	0.929
201	EM+AB	EM	AB	3.05	3	0.83	1.47	0.368	0.94	0.522	0.776	−0.128	−7.81	56.06	0.892
202	AB+EM	AB+EM	AB	17.17	3	0.81	15.31	2.718	0.83	0.867	0.222	0.168	10.63	14.38	0.829
204	AB	AB	AB	3.41	2	0.67	2.98	0.472	0.68	0.867	0.181	0.300	18.71	11.77	0.875
205	AB	AB	AB	18.35	4	0.68	9.96	1.649	0.71	0.874	−0.063	−0.029	−1.89	−4.13	0.769
209	EM+AB	EM	EM	13.15	8	2.82	3.26	1.000	3.08	0.542	0.516	−0.569	−37.26	43.58	0.884
210	AB	AB	AB	16.90	3	0.81	12.76	2.117	0.84	0.969	0.028	0.037	2.21	1.65	0.941
212	AB	AB	AB	3.59	2	0.30	3.05	0.472	0.30	0.907	0.114	0.233	14.31	7.16	0.890
213	AB	AB	AB	14.85	1	0.43	19.00	2.718	0.41	0.918	−0.043	−0.106	−6.57	−2.66	0.855
216	AB	AB	AB	10.86	2	0.71	8.65	1.284	0.74	0.980	−0.014	0.002	0.09	−0.84	0.961
218	AB	AB	AB	18.14	1	5.03	19.00	1.649	4.92	0.923	−0.222	−0.226	−13.38	−13.53	0.951
219	AB+EM	AB	AB	15.40	1	3.41	17.87	2.117	3.24	0.955	−0.153	−0.148	−8.72	−9.10	0.957
220	AB	AB	AB	18.74	2	2.28	14.86	2.117	2.17	0.955	−0.184	−0.168	−9.80	−10.89	0.973
221	AB	AB	AB	19.00	2	2.75	15.00	2.117	2.67	0.965	−0.146	−0.105	−6.16	−8.63	0.963
222	AB+EM	AB+EM	AB	9.99	4	0.72	2.87	0.472	0.76	0.882	0.221	−0.071	−4.47	14.07	0.832
223	AB	AB	AB	13.21	3	0.74	9.70	1.649	0.80	0.957	−0.069	0.038	2.29	−4.12	0.922

TABLE 2—*Continued*

				Spectral_1			Spectral_2			Principal Component Analysis Coefficients					
Fiber No. (1)	Line Strengths (2)	PCA (3)	Wavelet (4)	Age (Gyr) (5)	SF (6)	χ^2/ν (7)	Age (Gyr) (8)	τ (Gyr) (9)	χ^2/ν (10)	c_1 (11)	c_2 (12)	c_3 (13)	θ(14)	ϕ (15)	Radius^2 (16)
224	AB	AB	AB	16.00	2	1.64	13.82	2.117	1.62	0.966	−0.159	−0.143	−8.32	−9.33	0.980
225	AB	AB	AB	13.43	2	1.97	10.98	1.649	1.91	0.978	−0.128	−0.099	−5.75	−7.47	0.982
226	AB+EM	AB+EM	AB	2.87	2	0.34	2.42	0.368	0.34	0.764	0.256	0.266	18.25	18.50	0.719
227	AB	AB	PS	2.23	1	1.46	1.91	0.223	1.45	0.917	0.214	0.311	18.27	13.12	0.984
228	AB	AB	AB	7.30	1	0.44	9.37	1.284	0.42	0.976	−0.063	−0.010	−0.56	−3.69	0.956
229	AB	AB	AB	15.60	2	1.42	13.69	2.117	1.45	0.986	−0.090	−0.050	−2.90	−5.21	0.983
231	AB	AB+EM	PS	1.82	1	0.85	1.20	0.105	0.82	0.845	0.318	0.378	22.73	20.63	0.959
232	AB+EM	AB+EM	PS	18.77	6	0.81	3.42	0.607	1.08	0.854	0.403	0.065	3.97	25.25	0.895
234	AB	AB	AB	7.19	2	0.55	4.34	0.607	0.54	0.975	−0.040	0.078	4.56	−2.34	0.957
236	AB+EM	AB+EM	PS	2.40	2	0.97	2.19	0.368	1.01	0.871	0.375	0.125	7.54	23.31	0.915
237	AB	AB	AB	10.29	2	0.53	6.02	0.779	0.51	0.987	−0.104	−0.029	−1.70	−6.00	0.986
238	AB	AB	AB	3.13	1	0.47	3.05	0.368	0.46	0.985	−0.098	−0.021	−1.20	−5.67	0.980
240	AB	AB	AB	7.49	2	1.74	5.13	0.779	1.79	0.975	−0.154	−0.104	−6.00	−8.98	0.985
241	AB+EM	EM	EM	17.71	6	2.13	18.72	5.755	1.80	0.564	0.459	−0.304	−22.66	39.15	0.621
242	AB	AB	AB	12.87	2	1.74	10.80	1.649	1.78	0.989	−0.107	−0.047	−2.68	−6.18	0.992
243	AB	AB	AB	15.69	2	0.88	11.83	1.649	0.87	0.974	−0.168	−0.095	−5.52	−9.79	0.985
244	EM+AB	EM	AB	1.27	2	0.99	1.30	0.287	1.05	0.620	0.676	−0.005	−0.29	47.49	0.841
246	AB+EM	AB	AB	19.00	2	1.67	17.83	2.718	1.74	0.981	−0.006	−0.071	−4.14	−0.33	0.967
247	AB	AB	AB	2.93	1	0.52	3.24	0.472	0.50	0.968	0.084	0.188	10.97	4.98	0.980
248	AB	AB	AB	19.00	2	4.70	18.07	2.718	4.48	0.937	−0.174	−0.147	−8.78	−10.50	0.929
249	AB	AB	AB	9.88	2	0.93	8.31	1.284	0.95	0.961	−0.099	−0.037	−2.18	−5.88	0.935
250	AB+EM	AB+EM	AB	15.31	5	1.02	7.92	1.649	1.36	0.933	0.054	−0.224	−13.48	3.29	0.924
251	AB	AB	AB	2.86	2	0.30	2.43	0.368	0.31	0.821	0.096	0.208	14.10	6.69	0.727
252	AB+EM	AB+EM	AB	14.62	5	0.49	3.62	0.607	0.59	0.902	0.185	0.092	5.68	11.59	0.855
253	AB	AB	AB	19.00	4	0.49	12.14	2.117	0.53	0.940	0.014	0.125	7.56	0.85	0.899
254	AB	AB	AB	18.63	1	2.70	18.45	0.607	2.62	0.965	−0.164	−0.121	−7.03	−9.66	0.974
255	AB	AB	AB	16.10	4	0.50	4.00	0.472	0.51	0.959	−0.031	0.034	2.06	−1.85	0.922
256	AB	AB	AB	18.18	4	0.58	8.37	1.284	0.66	0.980	−0.034	0.036	2.10	−1.96	0.963
257	AB	AB	AB	18.68	4	0.50	10.00	1.649	0.56	0.969	−0.054	0.024	1.39	−3.18	0.943
258	AB	AB	AB	19.00	2	1.55	15.64	2.117	1.52	0.977	−0.131	−0.058	−3.34	−7.62	0.976
259	EM	EM	EM	2.76	8	11.34	2.68	2.117	9.45	0.016	0.680	−0.696	−45.65	88.64	0.948
260	AB	AB	AB	17.99	4	0.55	8.30	1.284	0.61	0.964	−0.022	0.044	2.60	−1.32	0.932
261	AB	AB	AB	14.72	1	1.96	17.50	2.117	1.87	0.960	−0.187	−0.162	−9.39	−11.03	0.984
262	AB	AB	AB	19.00	2	0.87	18.04	2.718	0.84	0.979	−0.141	−0.082	−4.75	−8.19	0.986
264	AB	AB	AB	17.01	2	0.84	14.23	2.117	0.87	0.985	−0.119	−0.040	−2.32	−6.87	0.985
266	AB	AB	AB	19.00	1	0.53	18.99	0.018	0.53	0.486	−0.032	−0.131	−15.01	−3.82	0.255
267	AB	AB	AB	16.87	4	0.61	3.49	0.223	0.68	0.957	−0.083	0.016	0.97	−4.98	0.922
268	AB	AB	AB	15.11	1	2.19	17.74	2.117	2.08	0.969	−0.162	−0.114	−6.63	−9.47	0.978
271	AB	AB	AB	19.00	4	0.78	8.77	1.284	0.82	0.969	0.023	0.160	9.39	1.34	0.964
272	AB	AB	AB	19.00	1	1.35	18.91	0.135	1.30	0.981	−0.139	−0.065	−3.76	−8.05	0.987
273	AB	AB	AB	16.35	2	1.38	12.04	1.649	1.40	0.978	−0.126	−0.075	−4.37	−7.33	0.977
275	AB	AB	AB	17.12	2	0.98	14.21	2.117	1.01	0.984	−0.087	−0.010	−0.55	−5.04	0.975
279	AB	AB	AB	2.79	2	0.93	2.39	0.368	0.98	0.962	−0.122	−0.006	−0.38	−7.24	0.940
280	AB	AB	AB	13.57	2	0.77	11.04	1.649	0.80	0.960	−0.183	−0.154	−8.97	−10.77	0.979

TABLE 2—*Continued*

				Spectral_1			Spectral_2			Principal Component Analysis Coefficients					
Fiber No. (1)	Line Strengths (2)	PCA (3)	Wavelet (4)	Age (Gyr) (5)	SF (6)	χ^2/ν (7)	Age (Gyr) (8)	τ (Gyr) (9)	χ^2/ν (10)	c_1 (11)	c_2 (12)	c_3 (13)	θ(14)	ϕ (15)	Radius^2 (16)
282	AB	AB	AB	3.05	1	0.22	2.50	0.004	0.22	0.839	−0.066	0.125	8.44	−4.47	0.723
285	AB+EM	AB+EM	AB	9.79	4	0.25	2.47	0.368	0.26	0.508	0.234	0.147	14.68	24.72	0.334
287	AB	AB	AB	18.61	2	0.95	14.82	2.117	0.95	0.962	−0.146	−0.043	−2.51	−8.65	0.949
289	AB	AB	AB	18.29	2	3.51	12.78	1.649	3.43	0.946	−0.173	−0.143	−8.45	−10.39	0.944
291	AB	AB	AB	12.25	4	0.41	3.24	0.472	0.44	0.951	0.035	0.121	7.24	2.09	0.921
292	AB+EM	AB+EM	AB	8.44	4	0.61	2.58	0.472	0.67	0.798	0.344	0.090	5.95	23.32	0.762
293	AB+EM	AB+EM	AB	1.90	2	0.80	1.66	0.287	0.86	0.818	0.368	0.086	5.46	24.19	0.812
294	AB+EM	AB	AB	17.72	5	0.94	5.90	1.000	1.27	0.962	0.138	0.067	3.93	8.15	0.949
295	AB	AB	AB	4.77	2	0.55	3.34	0.472	0.54	0.971	−0.047	0.094	5.55	−2.80	0.954
296	AB	AB	AB	7.43	1	3.04	8.40	1.000	2.99	0.962	−0.184	−0.108	−6.30	−10.82	0.971
297	AB	AB	AB	2.67	1	0.36	2.48	0.287	0.36	0.948	−0.102	0.080	4.78	−6.13	0.916
302	AB	AB	AB	4.42	2	1.55	3.75	0.607	1.59	0.948	−0.181	−0.208	−12.17	−10.79	0.975
303	AB+EM	AB	AB	16.67	2	1.25	16.45	2.718	1.35	0.956	−0.147	−0.126	−7.40	−8.75	0.952
304	AB	AB	AB	12.39	4	0.47	3.26	0.472	0.51	0.928	−0.109	0.020	1.20	−6.68	0.873
306	AB	AB	AB	7.14	2	0.41	4.32	0.607	0.41	0.972	−0.139	−0.054	−3.15	−8.11	0.967
307	AB	AB	AB	5.65	2	0.63	3.47	0.472	0.64	0.958	−0.009	0.106	6.34	−0.51	0.929
308	AB	AB	AB	2.00	2	0.41	1.72	0.287	0.43	0.924	−0.071	0.095	5.87	−4.39	0.867
309	AB	AB	AB	1.58	1	2.09	0.94	0.030	2.05	0.646	−0.246	0.030	2.48	−20.81	0.479
311	AB	AB	AB	1.55	2	0.86	1.28	0.223	0.93	0.883	−0.020	0.198	12.63	−1.27	0.820
312	AB	AB	AB	11.77	2	1.33	10.48	1.649	1.42	0.976	−0.140	−0.060	−3.49	−8.17	0.976

components. Our galaxy sample lies between these two extremes in terms of complexity and signal to noise, so this result is qualitatively consistent with these other works.

These first three eigenspectra are displayed in Figure 8. The first eigenspectrum represents the mean spectrum in our sample, so as expected it is a typical elliptical galaxy spectrum. It has spectral features typical of an old stellar population e.g., the strong absorption lines of Ca II H and K, *G* band, and magnesium. The second eigenspectrum contains strong Balmer absorption and emission lines, and strong [O III] emission. This component will clearly correlate with current star formation. The third eigenspectrum again contains strong Balmer absorption, but now the strong Hβ and O [III] lines are shown in absorption. The eigenspectra for eigenvalues beyond the top three components do not show major spectral features, so we believe these are mostly shaped by the noise in the data. Also, the eigencoefficients for these higher order components do not show any significant trends with our visual spectral types above.

7.2.3. *Galaxy Classification*

The eigensystem can be used to define eigencoefficients for each galaxy spectrum, which are simply the dot products of the galaxy spectrum with each eigenspectra. Since we are using uniform weights, the relationship is straightforward. For example, the $i^{\rm th}$ eigencoefficient of the $j^{\rm th}$ galaxy spectrum is simply

$$c_{i,j} = \sum_{\lambda} e_{\lambda,i}\, f_{\lambda,j}\,. \tag{5}$$

The resulting set of coefficients are normalized such that sum of their squares is one, that is, $\sum c_i^2 = 1$, where the summation index i runs through all eigencoefficients. In Figure 9, we show the distribution of the first, second, and third eigencoefficients. Immediately one can see that the different spectral types cluster into specific areas of eigenspace. The relationship between the three eigencoefficients is best related using a projection scheme as in Connolly et al. (1995), where three coefficients are converted into spherical coordinates. By assuming that all the useful information is contained within the first three components, we throw away the remaining coefficients and then treat the three top coefficients as a vector in a three dimensional space and convert them into a spherical coordinate system. In this view, the spectra can be described very simply by the two spherical angles θ and ϕ (see Fig. 10). The relative lengths of the vectors are not important for classification since they only represent how well each spectrum is represented by the three components.

Figure 10 shows the distribution of projected angles. The dashed lines show where we have made cuts based on the aforementioned classifications except that we have merged the EM + AB and EM types into one class. In Figure 11, we show the composite spectra from each of our four remaining classes (these composites are simply averages of the spectra). The cuts we have made in Figure 10 are arbitrary and were chosen to reproduce the line-strength classification scheme. The spectra have a continuum of possible shapes, which follow as a function of these parameters. Figure 10 shows that the angle θ correlates with the strength of the Balmer features in absorption and therefore can be used to differentiate poststarburst galaxies. The angle ϕ correlates with the emission-line strength and the K-star spectral features, thus being a good discriminator of the overall star formation activity. The dependence on the K-star spectral features can be seen in Figure 11 where we investigate a further division of the AB class into two subgroups ABa and ABb, along a line parallel to the PS boundary. The ABb class has stronger Balmer absorption but weaker Mg I and *G*-band features than does the ABa type.

We present the PCA classifications in column (3) of Table 2. For completeness, we also provide the coefficients of the PCA used in this paper: columns (11) to (13) contain the top three eigencoefficients, columns (14) and (15) are the θ and ϕ angle coefficients, and the square of the radius for each spectrum is given in column (16). We do not include any

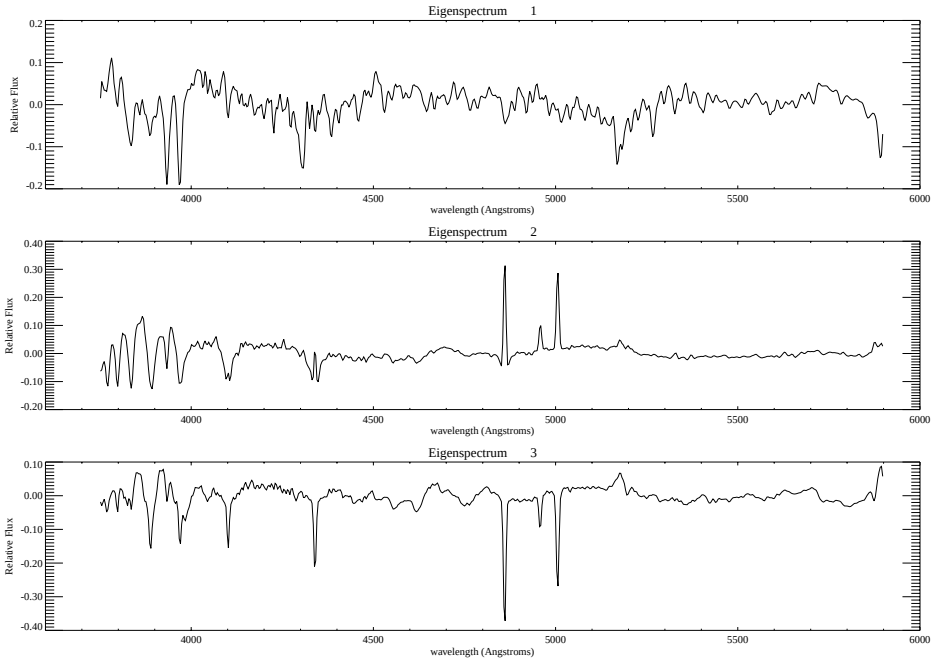


FIG. 8.—First three eigenspectra (see text)

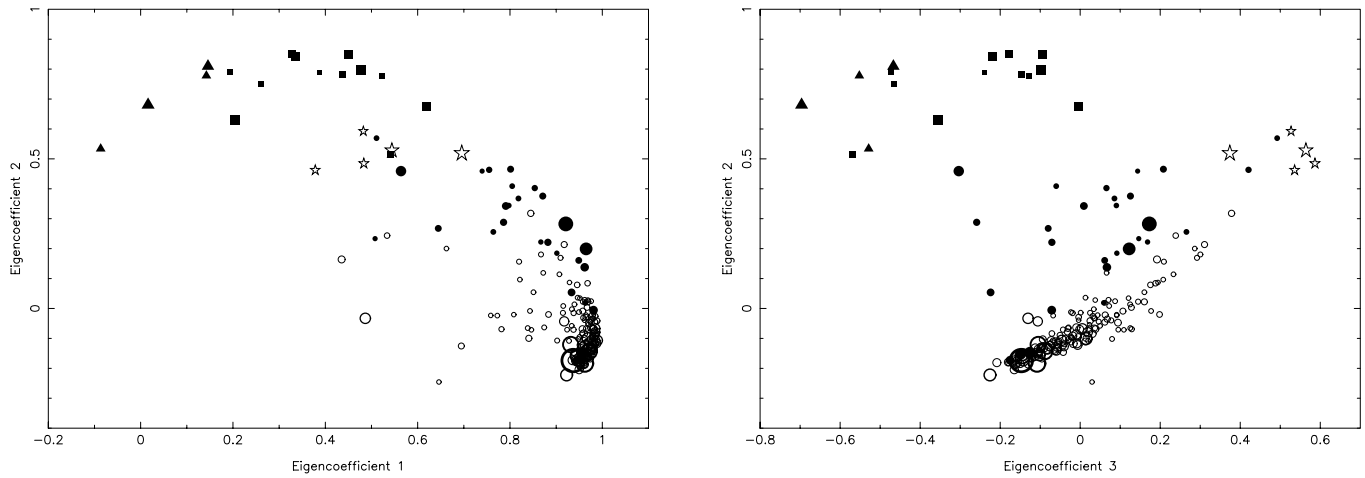


FIG. 9.—First three eigencoefficients. The symbols are our line-strength classification scheme; AB are open circles, AB+EM are solid circles, EM+AB are solid squares, EM are solid triangles, and PS are stars. The size of the symbol is proportional to the magnitude of the galaxy, as in Fig. 3.

information on the eigencoefficients in the case where the continuum is not subtracted as the results are qualitatively the same although quantitatively they differ.

7.3. *Wavelet Classification*

In addition to the PCA analysis on the Coma spectra, we have also investigated the use of wavelets, since they provide a multiresolution approach of classifying spectra that allows us to study—in a single analysis—both the small-scale emission/absorption features together with low-frequency continuum information. The goal of our wavelet analysis was to automate the line-strength classification given above using as few a number of wavelet coefficients as possible, thus providing an overall compression of information as well as producing an objective classification scheme that could be replicated elsewhere. For the analysis discussed herein, we have used the IDL Wavelet Workbench.[28] We do not provide here a detailed explanation of the theory behind the Wavelet since there now exists a large volume of literature on this subject (see, for example, Press et al. 1992).

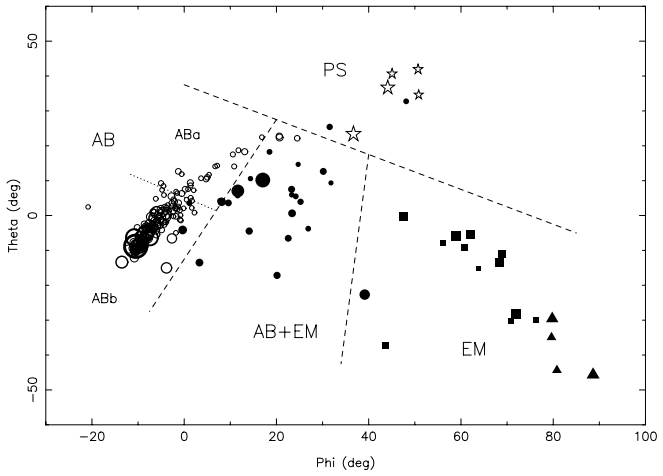


FIG. 10.—Plot of the spherical projection of the first three eigencoefficients. The plot symbols are the same as in Figs. 3 and 9. We show the cuts in eigenspace we have used to objectively classify our spectra. For this scheme, we have merged the EM and EM+AB types into the one type (EM).

To prepare the data for our wavelet analysis, analogously to the PCA analysis, we first shifted all spectra to the galaxy's rest frame and define a common (rest-frame) wavelength range (3890 → 5901 Å) which only uses data from the blue side of the SDSS spectrograph. We then computed the average pixel value for the whole spectrum and subtracted this off each pixel thus renormalizing the spectrum to have a mean of zero. This procedure removed the large discontinuities at the ends of the spectrum. The final step was to "zero-pad" the spectrum on either side of the data to create a pixel array with an integer power of two (2048 in this case). We then applied cosine-bell smoothing to the edges of the original spectrum to gradually taper the original data to zero thus avoid sharp edge-effects at the ends of the spectrum which would result in "ringing" or the Gibb's phenomena. For our spectra, we smoothed 5% of the original data at either end of the spectrum.

We note here that as in the PCA analysis above (§ 7.2), we did not use the red side of the spectrum because of the problems discussed in § 4 and thus we have no information about Hα in emission. However, for the wavelets, we did retain the shape of the continuum, unlike the PCA analysis. The multiresolution nature of the wavelets does not require continuum-subtracted data. Nonetheless, we also performed the same wavelet analysis with continuum-subtracted spectra obtaining different parameters values but a similar classification using the same strategy as described below.

We then performed a wavelet transform on these spectra which returned a series of wavelet coefficients at ten different resolution levels; the number of resolution levels is set by the size of the padded data array since each level has a factor of two lower resolution than the previous layer. An example of such a wavelet transform for one of the SDSS

[28] Based on Wavelab at Stanford University by Donoho, Johnstone, Buckheit, Chen, & Scargle. See ftp.rsinc.com/pub/user_contrib/wwb.

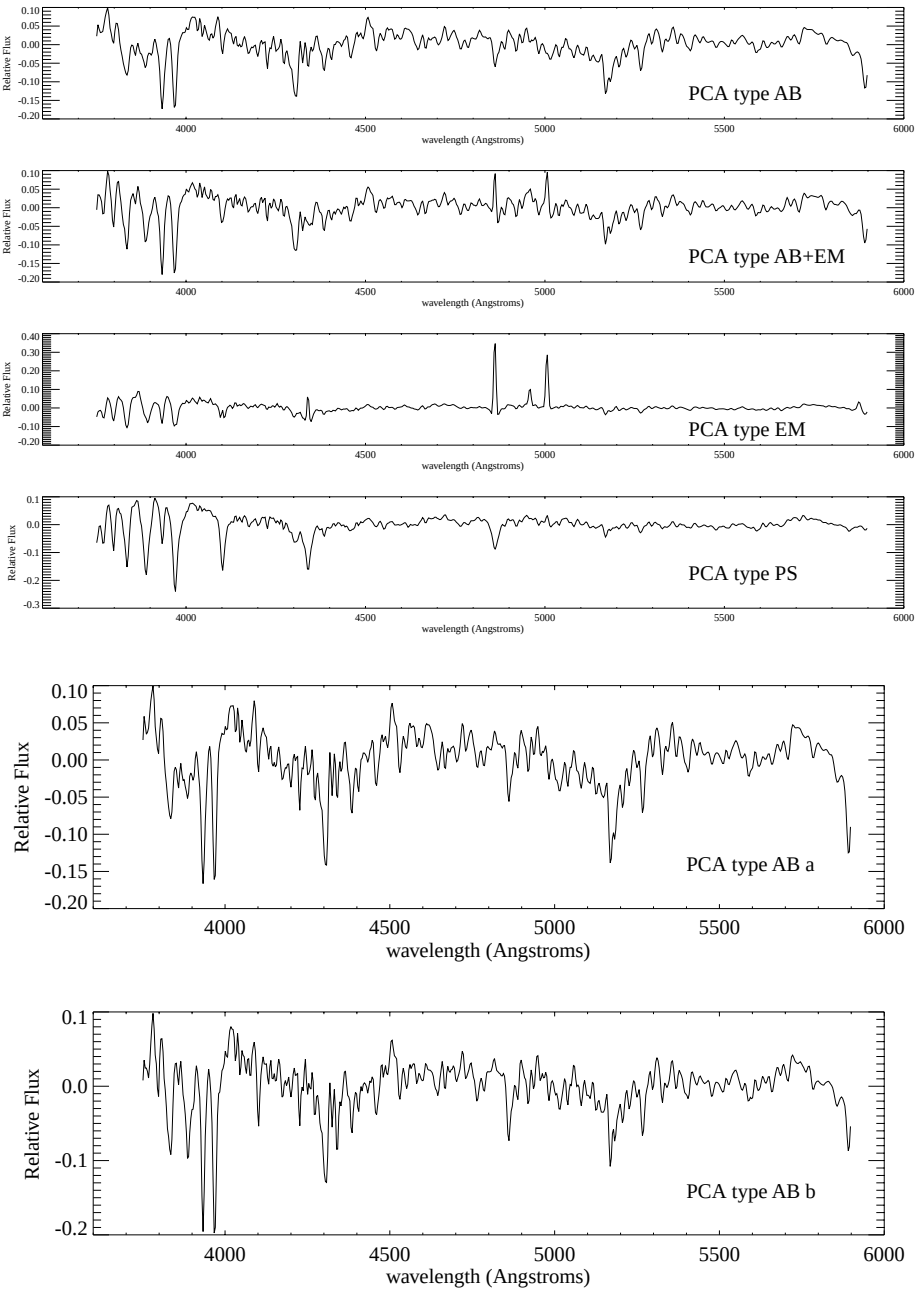


FIG. 11.—Composite spectra of the four PCA spectral types and the two sub-A types. The spectra for all the members of each group have been averaged with a uniform weight.

Coma spectra is shown in Figure 12 along with the different resolution levels and the corresponding amplitude of the wavelet coefficients at those resolution levels.

The first decision faced in the implementation of our wavelet analysis was the choice of the mother wavelet, e.g., a Daubechies, Symmlet, or Coiflet wavelet function. Moreover, we also needed to choose the level of smoothness for these wavelets, e.g., Daubechies2 (which is just a Haar wavelet), Daubechies4, Daubechies8, etc., with the higher numbered wavelets being smoother versions of the mother wavelet. To aid in these decisions, we performed a series of empirical tests on the data to determine which wavelet provided the maximal compression of the information for the smallest number of coefficients used in the reconstruction of the data. In these tests, we reconstructed the spectra using the largest N coefficients (in absolute value), regardless of which level they were taken from, as well as implementing the hard thresholding scheme; i.e., all coefficients below the N largest-valued coefficients were set to zero in the reconstruction.

In Figure 13, we show the measured mean χ^2 for all 196 Coma spectra as a function of N, the number of wavelet coefficients used in the reconstruction of the spectra. For our thresholding scheme, the Daubechies4 wavelet provided the most information compression, or largest fractional change in χ^2, for a given N coefficients. As expected, the χ^2 decreases exponentially as a function of N, and for small values of N the Daubechies4 clearly provides significant gain over the Symmlet wavelets. Therefore, we have used this mother wavelet (Daubechies4) in our analysis of these

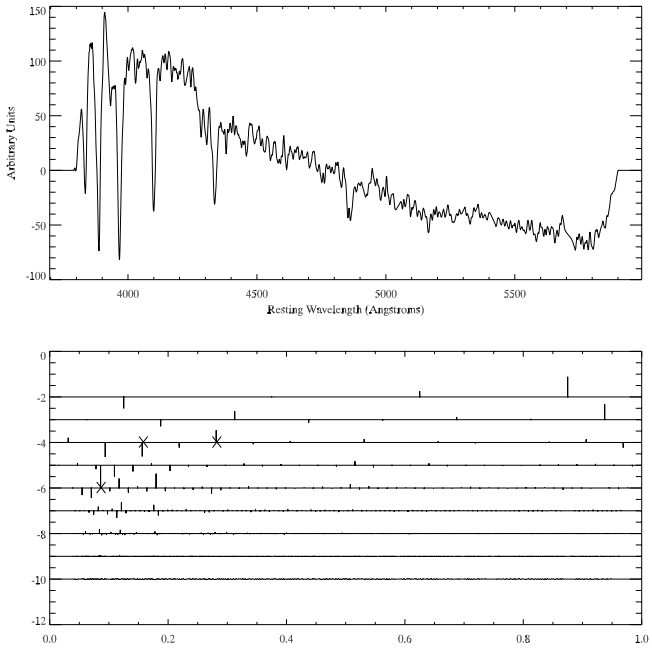


FIG. 12.—*Top*: Spectrum of one of the Coma poststarburst galaxies. We have subtracted off the mean pixel value as well as padded the ends with zeros to be 2048 pixels. Cosine-bell smoothing was applied to the ends to smoothly taper them to zero. *Bottom*: The different wavelet resolution levels start at the top with the lowest resolution and moving to higher resolutions toward the bottom of the figure. We show the relative height and sign of the wavelet coefficients. The crosses make the three wavelet coefficients used to classify this spectrum as a poststarburst (see text).

SDSS Coma spectra. This mother wavelet is rather sharp compared with the other wavelets which is an advantage for quantifying sharp discontinuities in these spectra such as the 4000 Å Balmer break discontinuity.

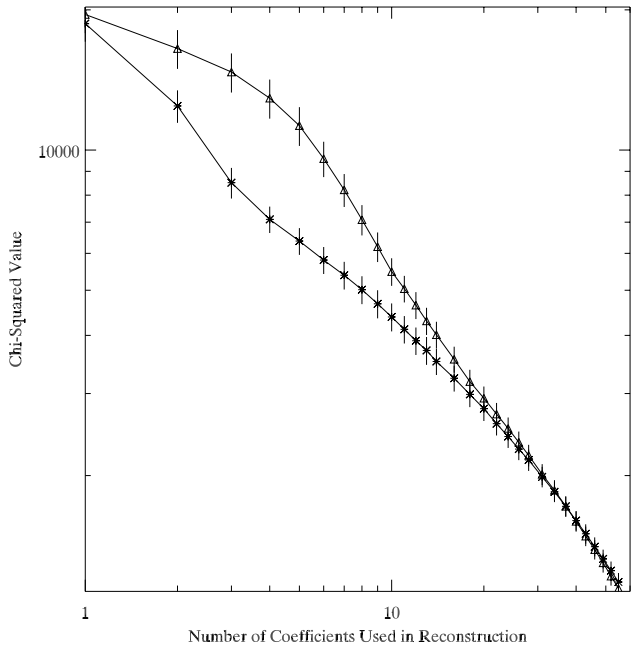


FIG. 13.—Mean χ^2 for all 196 Coma spectra for both the Daubeuchies4 (*stars*) and Symmlet8 (*triangles*) wavelets as a function of the number of wavelet coefficients used in the reconstruction of the spectra. The error is just the standard deviation observed between the Coma spectra. To avoid overcrowding, we have not plotted the similar curves for the Symmlet6 and Daubechies6 wavelets, since they are worse than those presented here (i.e., they have a higher χ^2).

We note here that we simply used the relative change in χ^2 to differentiate between the mother wavelets available, and the absolute goodness of fit from the χ^2 statistic is not being used because these spectral data are slightly correlated (because of the sky-subtraction and the resolution element being approximately 3 times the dispersion of these spectra). For reference however, we note that each spectrum had, on average, 2000 degrees of freedom (dof), and thus a reduced χ^2 equal to one, which suggests a reasonable fit between the model and observed data, is achieved after adding $\simeq 30$ wavelet coefficients (see Fig. 13). The fact we can explain these spectra with a relatively small number of coefficients agrees with our visual inspections and is reasonable given that we are studying a rather homogeneous subsample of galaxy spectra; i.e., a majority of the spectra are dominated by older spectral populations. We caution the reader not to overinterpret the absolute χ^2 results since we have not accounted for the correlations in the data.

In Figure 14, we plot the amplitude of the second and third largest wavelet coefficients for all 196 Coma spectra presented in Table 1. We have ignored the largest wavelet coefficient since it simply measures the amplitude of the whole spectrum and thus contains no information about the general shape of the spectrum (this is because a wavelet is defined to sum to zero). Figure 14 demonstrates that we can extract worthwhile information about these spectra from just two of wavelet coefficients; galaxies with recent star formation, as indicated by the presence of emission lines or poststarburst characteristics (A-star spectrum), preferentially possess large (negative) second and third wavelet coefficients, while absorption, non–star-forming, galaxies populate the remainder of the phase space. The explanation for Figure 14 is that these two wavelet coefficients are measuring the "color" of the continuum and are providing a similar discrimination as one may obtain from broadband

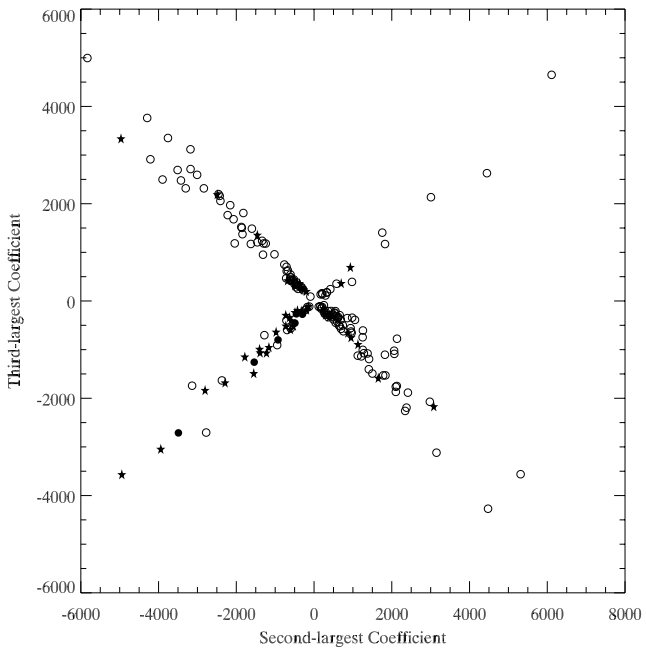


FIG. 14.—Second vs. third largest wavelet coefficient for all 196 Coma spectra. Open circles are absorption galaxies, solid triangles are emission-line galaxies, and solid circles are poststarburst (based on the initial visual classification). The "star pattern "seen in the distribution of these points is a product of our algorithm; i.e., the second coefficient must be larger (in absolute value) than the third coefficient.

multicolor photometry. This is exemplified by the fact that all the poststarburst galaxies in Figure 14 reside in the lower left arm since they all have "blue" spectra. In Figure 15, we show one of the poststarburst galaxies in Coma along with the reconstructed spectrum based on the three largest wavelet coefficients which illustrates that we have just measured the tilt of the spectrum. In this case, we have not exploited any high-frequency emission or absorption features, but have still managed to broadly segregate the galaxies based on their recent star formation histories.

To extend our analysis further, we have exploited the multiresolution nature of wavelets by designing an algorithm to classify galaxies as emission-line, poststarburst, and absorption-line galaxies using as few a number of wavelet coefficients as possible. Here, we have merged the different subdivisions of the emission lines as discussed in § 7.1 and focus on the AB, PS, and EM classes. To help define our algorithm, we co-added all the obvious poststarburst (PS) Coma galaxies (based on our visual classification scheme) and identified the strongest features in that co-added spectrum. In Figure 16, we show this summed spectrum and, as expected, the hydrogen Balmer absorption series is strong because of the young A stars in the galaxy. Also visible are the Calcium H and K absorption features (with the 4000 Å break Balmer discontinuity) which is indicative of an older stellar population (K-star spectrum). As discussed by Dressler & Gunn (1992) and Zabludoff et al. (1996) these poststarburst galaxies are also known as E+A or K+A galaxies, i.e., elliptical plus A-star or K plus A-star spectra.

The algorithm we have adopted is as follows. For each spectrum, we first scanned for the presence of any emission lines. This was empirically found to be equivalent to having one of the eight largest coefficients be a negative value located in the first five resolution levels, e.g., levels with more that 32 wavelet coefficients per level. We further restricted the search to look at wavelengths >4000 Å thus avoiding problems with the Balmer discontinuity.

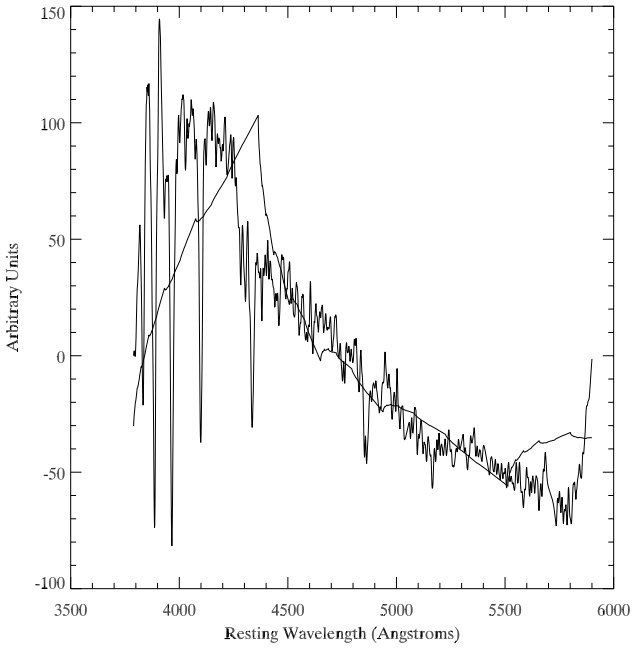


FIG. 15.—One of the strong poststarburst Coma galaxy spectra (same as presented in Fig. 12) and the wavelet reconstruction based on just the three largest wavelet coefficients (see Fig. 14).

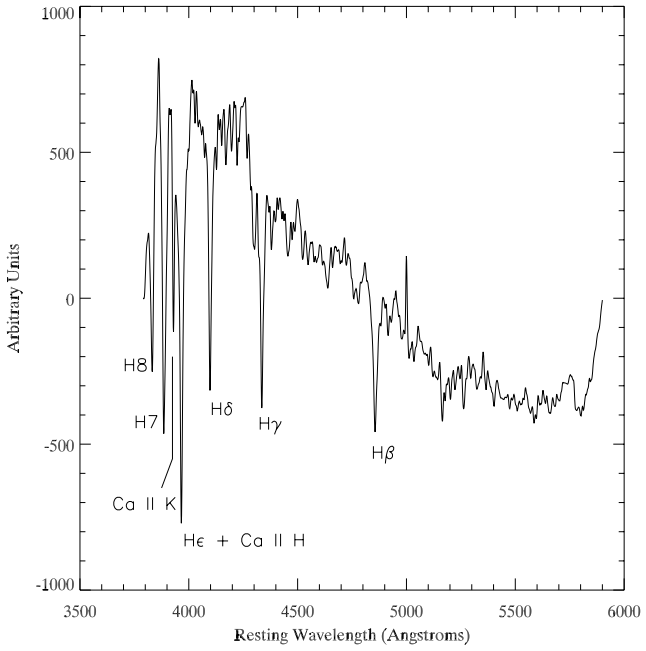


FIG. 16.—Co-added spectrum for six strong poststarburst galaxies visually identified in our SDSS Coma spectra. This plot illustrates the strong Balmer absorption features due to the young A stars. Also visible is the Ca II H and K absorption features common in older galaxies. We have labeled the common absorption lines.

To identify poststarburst galaxies, we then rescanned the first 12 largest coefficients for positive wavelet coefficients near the wavelengths of Hδ, Hγ, and H7 (see Fig. 12 for an example of this algorithm). These features were used since they are the strongest of the Balmer absorption lines as shown in Figure 16. We did not use Hβ because of possible contamination from emission especially if Hα is present about which we have no information in the current application of the method. If three such coefficients were detected, the galaxy was defined to be a poststarburst galaxy. We present these automated classifications in column (4) of Table 2.

7.4. *Synthetic Models*

As a final test, we have fit synthetic models of galaxy stellar populations to the Coma spectra. The advantage of this approach is that the spectra can be directly related to physical phenomena and parameters. The disadvantage is that the parameterization of the model, e.g., initial mass function (IMF) or the star formation history of the stellar population studied, can differ substantially from the real star formation processes thus introducing large uncertainties based on the particular model used. Moreover, it is difficult to compare this scheme with the aforementioned three empirical classification schemes. Despite these caveats, we present this work here which will be primarily used in a forthcoming companion paper.

Our method for comparing the stellar models with our Coma spectra is to minimize the following χ^2 function:

$$\chi^2(a_j) = \sum_{i=1}^{n} \left[\frac{F^{\lambda}_{i\,\mathrm{observed}} - F^{\lambda}_{i\,\mathrm{model}}(a_j)}{\sigma_i(F^{\lambda}_{i\,\mathrm{observed}})} \right]^2 , \qquad (6)$$

where a_j are the free parameters of the synthetic spectrum being fitted, i is an index running through pixels, $F^{\lambda}_{i\,\mathrm{observed}}$

and $F^{\lambda}_{i\,\mathrm{model}}(a_j)$ represent each pixel of the spectral energy distributions observed and modeled respectively and $\sigma_i(F^{\lambda}_{i\,\mathrm{observed}})$ is the error of the observed spectrum in pixel i.

In practice, the synthetic spectral energy distributions (SEDs) have a lower spectral resolution than our observed Coma spectra. Thus, we smooth both energy distributions to the same resolution; this means that the errors of the observed spectrum are therefore no longer uncorrelated. We also mask the spectral regions around strong sky emission lines to avoid the residual spikes coming from sky subtraction.

We used two sets of synthetic spectral energy distributions. First, we employed the evolutionary synthesis model PEGASE (Fioc & Rocca-Volmerange 1997) to generate the model spectra. We minimized the χ^2 using three free parameters: an overall normalization, the age of the stellar population and the star formation prescription. We assumed solar metallicity and did not fit for the internal extinction. The star formation prescription was parameterized using two different laws. (1) We assumed that the star formation rate (SFR) depends on the galaxy gas fraction as $\Phi(t) = \nu f_g(t)$, and we minimized with respect to the astration rate ν. In fact, we minimized this astration rate parameter using eight discrete values. Following Fioc & Rocca-Volmerange, we used the Rana & Basu (1992) IMF and values of the astration parameter that reproduce the colors of the different spectral-type galaxies observed locally. We also added a one gigayear starburst model. (2) We assumed an exponential SFR law $\Phi(t) = \tau^{-1} \exp(-t/\tau)$ and minimized with respect to the timescale τ. In this case, we used a standard Salpeter IMF with lower and upper mass limits of 0.1 and 120 $M_{\odot}$, respectively.

The age and star formation prescription of the best-fitting model spectrum are presented in Table 2. For the first SFR prescription we provide the age (col. [5]), the number of the best-fitting model (col. [6]), and the reduced χ^2 (col. [7]) of this best fit. The numbering of the models presented in column (6) is the following: number 1 corresponds to a one gigayear starburst model; numbers from 2 to 8 correspond to decreasing values of the astration rate parameter ν, where large ν values resemble star formation histories typical of early-type galaxies, and small ν values those typical of late-type galaxies. The degrees of freedom of the fit depend on the actual masking of each spectrum, but for the majority of them, there are 2005–2020 dof. We note here that our figure of merit, the χ^2 we compute, does not strictly behave as a real χ^2 distribution. It is certainly close to one, but not exactly, given that our errors have not been determined with high accuracy and there has been some smoothing which we have neglected, not taking into account the correlated nature of the errors. For the second SFR prescription, we present the age (col. [8]), the timescale τ (col. [9]), and the reduced χ^2 (col. [10]).

8. DISCUSSION AND CONCLUSIONS

8.1. *SDSS Spectroscopic System*

We present in this paper the first extragalactic spectroscopic data taken by the SDSS during the initial spectroscopic commissioning run in 1999 June. Although the data were primarily obtained to commission all the SDSS spectroscopic subsystems (guider, plug plates, spectrographs, control software) and are therefore far from the nominal quality seen for the main SDSS survey, these Coma spectra are of reasonable quality and provide a new insight into the galactic content of the Coma cluster, especially at large distances from the cluster center. This is a combination of the high throughput of the SDSS spectrographs, the large field of view of the spectroscopic observations (3° diameter), the extensive wavelength coverage and resolution, and the ability to obtain many hundreds of spectra simultaneously. This single plug-plate observation of Coma illustrates the overall efficiency of the SDSS spectroscopic system and demonstrates the potential for further cluster and field galaxy observations.

As of 2000 December the entire SDSS spectroscopic system has been tested and commissioned. Both spectrographs are operational and are routinely collecting data. The target selection procedure, from determining target objects from SDSS photometry through to drilling plug plates and shipping them to APO, has been exercised several times and the emphasis has now shifted to improving the overall efficiency of the observations. At the timing of writing, the SDSS has obtained $\simeq$90,000 spectra (approximately two-thirds galaxies and one-third quasars) and these data are being used, among other things, to define our integration time, completeness limits, as well as to debug the SDSS spectroscopic software. These data also represent one of the largest samples of galaxies and quasars presently in existence and are being used for several scientific programs.

We have obtained 320 spectra (half the number of a nominal SDSS plug plate) in the central region of the Coma cluster. The availability of one spectrograph only allowed us to observed the southern half of plate 133 (see Fig. 3). Other engineering tasks and bad weather conditions prevented us from obtaining further Coma spectra and future data taken in this region will be acquired as part of the regular SDSS survey (both imaging and spectroscopy). Nevertheless, in 1 hour of observations with only half of the spectroscopic system commissioned and without optimizing the target selection, we obtained 196 spectra of Coma galaxies. This number represents approximately one-third of the number of redshifts presently available in the literature within the same 1.°5 radius from the cluster center (as estimated from the NED database in 2000 August). Among the 320 fibers available, 11 were placed on blank sky (to allow sky subtraction from the rest of the fibers), while the rest of the science fibers yielded 196 Coma galaxy spectra, 49 field galaxies, five quasars (which were previously known and targeted on purpose), 47 stars, and 12 unidentified spectra. Four of the unidentified spectra were due to "spill-over" from bright adjacent fibers.[29] We note here that our target selection attempted to maximize the number of available galaxy targets by including all candidate galaxies, i.e., galaxies that were only classified as galaxies on one of the two photographic plates scanned by SuperCOSMOS. In hindsight, this produced considerable stellar contamination, even at bright magnitudes, but does ensure a higher level of completeness.

Of the 196 Coma redshifts obtained, 45 represent new identifications. Because of the large, circular field of view of the SDSS, these new redshifts are located at large cluster

[29] Fibers are only separated on the CCD camera by approximately 6 pixels. The FWHM of a fiber on the CCD is approximately 2 pixels. Therefore, the light from bright target fibers can *contaminate* adjacent fibers.

radii in areas scarcely sampled by other spectroscopic surveys of Coma. Given this uniformity and the quality of our data, we are thus able to obtain a better understanding of the spatial distribution of galaxy types within Coma.

For the 151 redshifts found in common with the literature, we found a negligible mean offset between our redshift determinations and those already published. In particular, when we compared our redshifts with the largest homogeneous sample of redshift available in the literature, the 63 galaxies measured by CD96, we found only a 3 km s^{-1} mean offset with an rms scatter of only 24 km s^{-1}. This is remarkable given the nonoptimal observing conditions, the lack of proper calibration frames, the difference in the spectral resolutions of the two instruments used, as well as the nonstandard wavelength calibration used. Moreover, we have looked for correlations between the observed difference between CD96 and our redshift as a function of CCD position, plate position, and matching distance, and we find no significant dependences on these observational parameters. In summary, it is likely that we have overestimated the error due to our wavelength calibration, given the low rms difference with CD96; the SDSS spectroscopic systems appear to be remarkably stable and linear over a 1 hour observation.

8.2. *Dynamics and Spectral Classifications*

In Figure 5, we show the redshift distribution of our 196 Coma members, which is qualitatively similar to that seen for the 465 redshifts in CD96 (their Fig. 5). This is not surprising since we have 148 galaxies in common with their analysis. However, we do sample out to larger radius than CD96, and the fraction of galaxies measured in the NGC 4839 group (in the southwest portion of the cluster), with respect to the total, is larger in our sample than in CD96. A single Gaussian fit to our data gives a mean velocity of 6950 ± 66 km s^{-1} and a velocity dispersion of $\sigma_v = 916 \pm 50$ km s^{-1}, where we have corrected for the fact that we measure the velocity dispersion with a 3 σ clip criterion. These values are in agreement with previous measurements and, as expected, are an average of the mean velocities, and mean velocity dispersions, of the main cluster core and the NGC 4839 group (see CD96). As already noted by CD96, a single Gaussian fit to the data is an oversimplification with a clear excess of galaxies, compared with the single Gaussian, between $\simeq 6950 \rightarrow 7600$ km s^{-1} due to the NGC 4839 group. The central velocity of these excess galaxies is approximately coincident with the mean redshift quoted by CD96 for the NGC 4839 group, 7339 km s^{-1}. We have also investigated the dynamical differences between the absorption-line galaxies and the active (emission-line and poststarburst galaxies) galaxies. We find that the AB galaxies given by the line-strength classification have a mean velocity of 6923 ± 70 km s^{-1} and a velocity dispersion of $\sigma_v = 846 \pm 54$ km s^{-1}, while the rest of the galaxies have $\langle cz \rangle = 7027 \pm 160$ km s^{-1} and $\sigma_v = 1160 \pm 134$ km s^{-1}. The velocity dispersion of the active galaxies is then 30% higher than that of the absorption-line galaxies. This is similar to the difference found by CD96 for Coma and Carlberg et al. (1997) when comparing the velocity dispersions measured from the red and blue galaxies in the CNOC1 cluster survey. We defer a more detailed examination of the dynamics of the whole Coma region until the future when we have both high quality photometric and spectroscopic data from the main SDSS survey in hand.

In this paper we present several different spectral classifications for our 196 Coma galaxies. The homogeneity and quality of the data allowed us to experiment with these different classification schemes to understand their applicability to the main SDSS survey. The first classification scheme was based on the presence or absence of emission lines. In this case, the Hα line served as the main classifier. For typical IMF and metallicities, Hα cannot be detected in emission ~ 25 Myr after the end of active star formation. Therefore, this criterion efficiently separates galaxies with current star formation from those without. The strength of the Hβ line in emission, and the strength of the Hδ, Hγ, and Hβ in absorption, are used as additional diagnostics to improve the classification (see § 7.1). Using these specific lines, we were able to subdivide the galaxies into five spectral types, which we discuss below.

Soon after the termination of a star formation episode, even if it only includes a few percent of the stellar population, the blue part of the optical spectrum of a galaxy is dominated by A stars, which are characterized by the Balmer absorption features. If there is no further star formation activity the strength of these lines diminishes gradually with time. The Balmer absorption lines strength thus provides a rough estimate of the age of the stellar population, although the lines are also somewhat sensitive to metallicity. We use this criterion to separate absorption-line systems into two subclasses. Galaxies without recent star formation, based on the absence of Hα in emission and the absence of strong Balmer absorption, were classed as AB. Galaxies in which their last episode of star formation ended recently, or poststarburst galaxies (PS), were characterized by their strong Balmer absorption lines as well as the absence of Hα in emission. The threshold between AB and PS was set at an equivalent width larger than 15 Å for the sum of Hδ, Hγ, and Hβ equivalent widths. This corresponds to roughly 400–700 million years after the truncation of the active star formation for solar metallicity. We note here that our criteria are based on equivalent widths; thus this threshold also depends upon the underlying stellar population (or the previous star formation history), i.e., how many stars are contributing to the continuum. Emission-line galaxies were divided into three subclasses (AB+EM, EM+AB, and EM) depending upon the strength of the Hβ line. The W_o(Hβ) cuts are difficult to translate into star formation rates, given the different continuum strengths and the fact that we have not attempted to correct the intrinsic extinction. Nevertheless, the equivalent width of Hβ represents a measure of the strength of the star formation process with respect to the underlying stellar population.

This classification scheme has the advantage of being simple and easy to measure in optical spectra with sufficient wavelength coverage, and it is meaningful as it classifies spectra according to their star formation activity relative to the overall stellar population. Undoubtedly, the use of Hα, instead of Hβ, to subdivide the emission-line spectra would have been preferred, as it is a better indicator of star formation and is less affected by extinction. However, the nature of our data made us settle for Hβ. We can use this classification as the test base with which to compare our other schemes.

Other classification schemes based on spectral features have also been used in the literature. In particular, the MORPHS group (Dressler et al. 1999; Poggianti et al. 1999) and the CNOC group (Balogh et al. 1999) have recently put

forward similar classification schemes based on the [O II] and Hδ lines, in which they provide a more physical interpretation of their types based on evolutionary spectral synthesis models. They use the [O II] and Hδ lines as indicators of current star formation and the time elapsed after the last episode of star formation, respectively. The large wavelength coverage of our spectra allow us to use more spectral features, Hα, Hβ, Hγ, and Hδ, for the same purpose. Here, we have taken the phenomenological approach of providing a simple classification scheme based on observational quantities which are directly related to the star formation processes taking place within galaxies. We defer to a future paper a more detailed interpretation of these classes in terms of the evolutionary phases of galaxy stellar populations.

There are 44 galaxies (22% of our sample) which show evidence of current star formation to some degree. There are five extra galaxies, classified as poststarbursts, which ceased their star formation process in the last $\sim$500 Myr. If we include these five galaxies into the active galaxy population, then 25% of our galaxy sample show some sign of recent star formation activity. In Figure 3, we show the spatial distribution of all 196 Coma galaxies; the plotting symbol type reflects our line-strength classification scheme discussed above and in § 7.1. Clearly, there is no obvious correlation in the position of the different types of galaxies except that the active star-forming galaxies avoid the cluster center.

In addition to the line-strength classification scheme, we have explored two objective schemes based on PCA and wavelets. For our PCA analysis, Figure 7 shows that the first three eigenspectra for our data set contains 87% of the variance while most of the remaining variance is likely due to the noise in our spectra. Each spectrum can therefore be expressed as a linear combination of these three eigenspectra which in turn can be presented in a spherical coordinate system with only two important parameters (see Fig. 10). We have defined regions in this two-dimensional space according to our line-strength classification scheme.

In Table 3, we compare the line-strength and PCA classifications to check whether the two-dimensional space defined by the eigencoefficient projection angles can be understood in terms of the absorption and emission lines of the spectra. The agreement between both classifications is obviously good but nevertheless remarkable as there was no a priori guarantee that such a good separation should be achieved given that the PCA classification is based on the overall continuum-subtracted SED, while the line-strength classification only on the Balmer lines. Figure 10 demonstrates that simple arbitrary cuts can efficiently separate galaxies according to their spectral line strengths. The only cut which does not clearly reproduce the line-strength classification above is the division between AB and AE galaxies.

TABLE 3

LINE STRENGTHS VERSUS PCA CLASSIFICATION

PCA\Line Strengths	AB	PS	AB+EM	EM+AB	EM	Total
AB	144	0	6	0	0	150
PS	0	5	2	0	0	7
AB+EM	3	0	19	0	0	22
EM	0	0	1	12	4	17
Total:	147	5	28	12	4	196

In fact this is mostly due to fact that we have used Hα to split these two classes in the line-strength classification but have only used the blue part of the spectrum in the PCA analysis. Some of these galaxies show Hα in emission while the rest of the Balmer series is seen in absorption. PCA thus classifies the galaxy as an AB galaxy while in the line-strength classification it is an AB+EM galaxy based on the presence of faint Hα emission. In addition, two galaxies classified as AB+EM by their line strengths are classified as PS by the PCA analysis (fibers 91 and 140). Both galaxies show strong broad Balmer absorption features which are filled with narrower emission. In these cases, it is difficult to measure the absorption- and emission-line components equivalent widths separately. We estimate that galaxy 91 has $W_o(\mathrm{H}\delta + \mathrm{H}\gamma + \mathrm{H}\beta) \sim 10$ Å in absorption and galaxy 140 has $W_o(\mathrm{H}\delta + \mathrm{H}\gamma + \mathrm{H}\beta) \sim 15$ Å. The latter would have been classified as a PS galaxy by the line-strength criteria if it did not have the emission. These two galaxies have certainly experienced star formation activity that has been substantially decreased in the last gigayear, giving rise to the strong Balmer absorption lines. However, there is still some residual star formation activity going on, and thus the weak emission on top of the absorption.

We have used a version of the PCA based on the implementation presented in Connolly et al. (1995) and Connolly & Szalay (1999). Our method uses the data themselves to generate the eigenbasis in which the observed spectra are projected. We then use another classification scheme, the line-strength classification, to subdivide the eigencoefficent parameter space according to it. The line-strength classification can be translated strikingly well into separated regions on the two-parameter space given by the angles θ and ϕ. Other classification schemes employing PCA have also been used in the literature. For example, Bromley et al. (1998) use a PCA to classify the Las Campanas Redshift Survey. Their implementation is very similar to ours. They use the data themselves to generate the eigenbasis as we do. They weigh their spectra by a smoothed version of the mean spectrum, while we continuum-subtract each spectrum with a low order polynomial. Their sample is composed of field galaxies instead of galaxy cluster members and therefore their first eigenspectrum (their Fig. 1) is more emission-line–dominated. Unlike us, they only use their first two eigencoefficients to classify their spectra, neglecting the third eigencoefficient that appears to be able to differentiate poststarburst galaxies. They subdivide their two eigenspectra parameter space into six "clans" or spectral types, without using any other external classification scheme for that subdivision. Their mean spectra for their clans show (their Fig. 3), nevertheless, a good correlation with star formation. Poststarburst galaxies are, however, not represented. Folkes et al. (1999) classify a preliminary sample of the 2dF galaxy survey using a PCA as well. Their sample is made up of field galaxies. Their PCA implementation is similar to us except that they subtract a mean spectrum from their spectra before applying the PCA. Their eigenspectra (their Fig. 5) reflect both facts with their mean spectrum being similar to our first eigenspectrum (modulo our continuum subtraction), their first eigenspectrum being similar to our second and their second similar to our third. They use another external classification to subdivide their first two eigencoefficient parameter space to generate their classification. They argue that their third eigencoefficients do not add much additional information for their classification

scheme. The ESO-Sculptor Survey has also been classified with a PCA method by Galaz & de Lapparent (1998). They employ the Connolly et al. (1995) implementation, that is, the same method we use. Again, their eigenspectra are more emission-line–dominated than ours as they study a field galaxy population. They decompose their spectra into the same projection angles we do. However, they classify their spectra comparing them with the Kennicutt (1992) spectra projected onto the same eigenbasis generated by the data themselves. They find that their spectra can be interpreted as a one parameter family in their θ-ϕ space. Their sample is of comparable size and signal-to-noise to ours but of coarser resolution. On the other hand, both Bromley et al. (1998) and Folkes et al. (1999) samples are larger and contain noisier spectra than ours. Their classification (as well as Galaz & de Lapparent's) rely on the spectra being a one parameter family going along stellar activity strength. Our spectra, however, being a cluster sample, has more absorption-line galaxies and more poststarburst galaxies that require another parameter to be differentiated from the star forming sequence. We argue that our classification requires two parameters: one, describing the stellar formation activity; the other, the strength of the Balmer absorption features.

There have been other approaches to construct classification schemes using PCA. Connolly et al. (1995), Connolly & Szalay (1999), Sodré & Cuevas (1997), and Ronen et al. (1999) use spectral synthesis models (or galaxy spectra already classified) to construct their PCA eigenbases. They, then, interpret their classifications in terms of their input, either their already classified spectra or the synthesis model parameters. Given that spectral synthesis models currently available do not have the spectral resolution of our observed spectra, we have chosen to use our own spectra to build our eigenbasis and apply the line-strength classification to subdivide the eigencoefficient parameter space. Therefore, not losing the spectral resolution of our data.

We have also used wavelets to define a simple classification for these spectra which uses both the absorption and emission lines in conjunction with the continuum shape. As with the PCA analysis, we only utilize the blue part of the spectrum and thus have no information on Hα. We also do not try and differentiate between the EM, AB+EM and EM+AB line-strength types since, at present, we cannot measure the equivalent width of lines directly from the wavelet analysis (although in principle this could be achieved). In Table 4, we compare the wavelet classification with the line-strength classification. As above, there is good agreement between the two where the line-strength subclasses of AB+EM and EM+AB classifications are mostly shared between the EM and AB wavelet classes (19 AB+EM galaxies were placed in the wavelet AB class as expected since there is no information about Hα). The only surprises in Table 4 are the four galaxies (fibers 84, 138, 201, and 244) classified as AB in wavelet space but EM+AB by the line-strength criteria. A visual inspection of these spectra shows that the signal-to-noise of these data is, on average, low. However, all four have moderately weak emission lines that probably missed the top 8 wavelet coefficients because of their size. All four do have strong Calcium H & K indicative of an old stellar population. We also note that the wavelet algorithm has more PS galaxies than the line-strength classification. This is primarily due to the hard threshold of $W_o(\mathrm{H}\delta+\mathrm{H}\gamma+\mathrm{H}\beta) > 15$ Å imposed in the line-strength classification. These extra wavelet PS galaxies (three classified as AB and 7 as AB+EM galaxies by the line-strength method) do have Balmer absorption lines, but either they have Hα in emission and/or the Balmer absorption is weak (although still stronger than galaxies dominated by old stellar populations). This apparent discrepancy in the classification schemes can be easily understood in terms of the thresholds used in assigning the PS classification, i.e., if the 15 Å threshold used in the line classification scheme had been lowered, then many of these galaxies would have also been classified as PS by the line-strength scheme. The wavelet scheme has simply picked extra *older* poststarburst galaxies with weaker Balmer absorption lines.

In Table 5, we show the cross-comparison between the PCA and wavelet classifications. Again, the agreement is very good. The only exceptions are the same cases discussed above given that the PCA classification cuts were applied to reproduce the line-strength classification. It is worth mentioning here that the extra wavelet PS classified galaxies discussed above reside in the "bridge of galaxies" that join the AB and PS regions shown in Figure 10. This again explains why we find more wavelet classified PS galaxies compared with the other schemes since we are simply sampling more of the galaxy population between these two classes.

We have also fitted evolutionary spectral synthesis models to our Coma spectra (only the blue side of the spectrum) to understand the composition and history of the stellar populations in these galaxies. We note that these fits are performed for a particular model, with a chosen star formation prescription, and should be interpreted as such. The star formation history of a galaxy is more complex that the simple parameterized models used (e.g., Abraham et al. 1999) and the best fit gives only an indication of the properties of the combined stellar population and helps to compress the spectral information into a handful of meaningful parameters.

We have chosen to fit the age of the stellar population and a parameter describing the star formation prescription using two families of models (see § 7.4 for further details). Both parameterizations give similar results (see Table 2). It is nevertheless clear from Table 2 that in some cases the star formation prescription utilized is unable to fit properly the

TABLE 4

LINE STRENGTHS VERSUS WAVELET CLASSIFICATION

Wavelet\Line Strengths	AB	PS	AB+EM	EM+AB	EM	Total
AB	144	0	19	4	0	167
PS	3	5	7	0	0	15
EM	0	0	2	8	4	14
Total:	147	5	28	12	4	196

TABLE 5

PCA VERSUS WAVELET CLASSIFICATION SCHEMES

Wavelet\PCA	AB	PS	AB+EM	EM	Total
AB	148	0	15	4	167
PS	2	7	6	0	15
EM	0	0	1	13	14
Total:	150	7	22	17	196

observed spectrum and a different prescription with combinations of different bursts is necessary. We have chosen, at this stage of simple comparison with other classification schemes, not to fit for the intrinsic absorption or the galaxy metallicity, assuming fixed solar metallicity and no intrinsic absorption. Indeed, there are known degeneracies between age-metallicity and age-intrinsic absorption when fitting synthesized SED to observed spectra (e.g., Worthey 1994; Thompson, Weymann, & Storrie-Lombardi 2001). In general, a higher metallicity and the effect of neglecting internal extinction will be compensated by an older computed age.

Figure 17 presents the age and timescale, τ, of the best-fit synthesized SED using an exponential SFR law. The symbols represent the different line-strength classifications while the size of the symbol represented the observed magnitudes of the galaxies. Most of the Coma galaxies cluster along a strip in the age-τ space. The large dynamic range shown for the τ parameter gives the impression that galaxies of different line-strength classes populate similar regions in this parameter space. However, the general trends of age-τ values with respect to the spectral line-strength classification are as expected: AB galaxies populate regions of old ages ($\geq$3–4 Gyr) and short timescales of star formation which produce old stellar population while the AB+EM, EM+AB and EM galaxies occupy regions next to the AB galaxies but gradually moving to younger ages and longer τ as the emission-lines strength increases. Finally, the PS galaxies populate the region of short timescale star formation, which correspond to short and intensive star formation histories, and short ages after the strong formation episode. To help visualize these separate regions of the age-τ space, we show in Figure 18 the 1, 2, and 3 σ contours of the age-τ regions occupied by three representative galaxies drawn from our three main spectral types, i.e., an AB type galaxy (fiber 143), a PS type galaxy (fiber 95), and a EM+AB type galaxy (fiber 117). It is clear from this plot that the AB and EM+AB galaxy inhabit different regions of the age-τ space (at the 3 σ level), while there is no intersection for the AB and PS galaxies either. Only the EM+AB and PS galaxies share a similar parameter space (at the 3 σ level). Nevertheless, it is clear from Figures 18 and 17 that the fits of the exponential decaying star formation models to the observed spectra are degenerate along a line in the log *tau*–log age parameter space of slope $\sim$3/2. In summary, regardless of this degeneracy, our spectral classifications have a broad relationship to expected physical models of star formation and therefore, they can be used to study star formation and galaxy evolution with the Coma cluster.

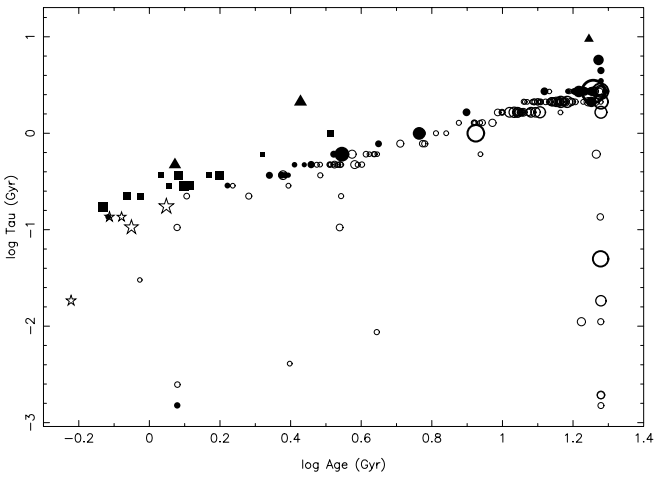


FIG. 17.—Star formation prescription vs. age for all Coma galaxies (see text). The maximum allowed age in the minimization is 19 Gyr.

8.3. *Galaxy Star Formation in Coma*

Our analysis of the Coma cluster has revealed that a substantial fraction (25%) of galaxies in Coma (out to the virial radius) exhibit recent star forming activity. Such analyses are at the heart of studies of galaxy evolution in clusters and, in more general terms, the Butcher-Oemler (BO) effect (Butcher & Oemler 1984). Our large fraction of recent star-forming galaxies is more than initially expected for such a low redshift cluster but is in reasonable agreement with other spectroscopic studies of galaxy star formation in clusters. For example, Caldwell & Rose (1997) found that $\sim$15% of galaxies in five nearby clusters showed signs of recent star formation while the work of Ellingson et al. (2001) shows that $\sim$20% of galaxies within the virial radius ($\sim r_{200}$) of CNOC1 clusters ($0.18 < z < 0.5$) show signs of recent star formation. However, we do not address here the redshift dependence of the BO effect since that will require a large, homogeneous sample of clusters spanning a significant range in redshift (see Andreon & Ettori 1999; Margoniner & de Carvalho 2000). We will address this issue using the main SDSS sample.

We explore here possible mechanisms for triggering star formation in clusters of galaxies. Several authors (Burns et al. 1994; Caldwell & Rose 1997; Metevier, Romer, & Ulmer 2000; Wang, Connolly, & Brunner 1997) have proposed that shocks caused by cluster merger events can trigger star formation in cluster galaxies. However, Figures 3 and 19 show that our Coma galaxies with recent star formation (EM+AB,AB+EM, EM, and PS) are random distributed throughout the cluster with no apparent correlation with the NGC 4839 group. This implies that this merger (or postmerger) has had little effect on the recent star formation rates of Coma contrary to the scenario outlined in Burns et al. (1994) and Caldwell & Rose (1997). This difference may be the combination of several effects. (1) We have a complete, homogeneous, spectroscopically confirmed, sample of Coma galaxies out to large cluster radii, i.e., we have targeted all bright galaxies out to the virial radius of Coma regardless of their location, color, or morphological type. Caldwell & Rose (1997) were forced to selectively sample specific areas in Coma, because of the smaller field of view of their instrument, as well as preferentially targeting early-type galaxies. (2) We have used different schemes and thresholds for defining poststarburst and star-forming galaxies. For example, if we lowered our threshold for the definition of a PS galaxy (to older and weaker lines), we may find a correlations with the NGC 4839 group. We note however that the extra wavelet PS galaxies (which are older PS galaxies) show no sign of excess clustering with the NGC 4839 group. (3) The NGC 4839 is approximately 5%–10% (CD96) of the mass of the core of Coma and thus the merger of Coma and this group may not be severe enough to trigger the levels of star formation seen in more extreme head-on cluster-cluster and group-group mergers (Metevier et al. 2000). (4) If the NGC 4839 group is still "spiralling" into Coma then we could simply be seeing the combination of ram-pressure induced star formation as the field galaxies first infall into the cluster (see Dressler & Gunn 1983), as

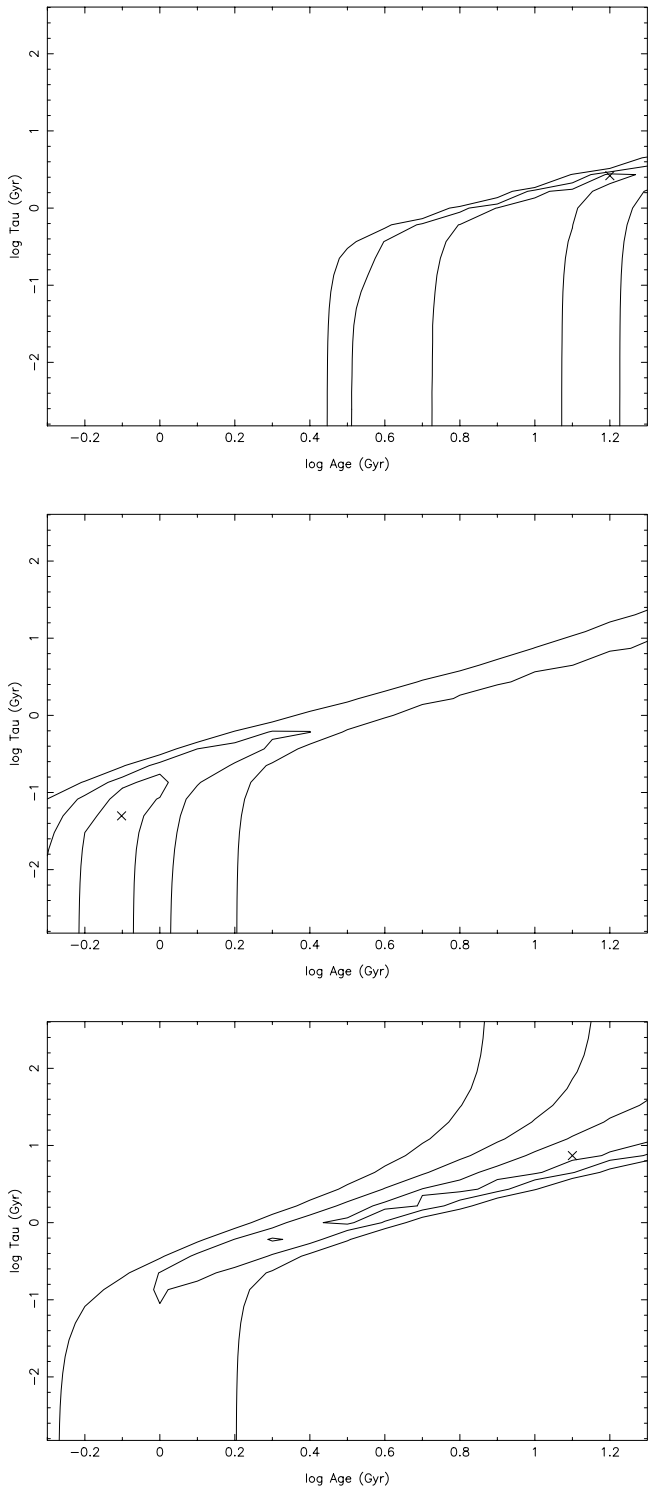


FIG. 18.—1, 2, and 3 σ confidence levels contours for the spectral fit of three galaxies of different type. The cross signals the best-fit age and τ parameter. *Top*: fiber 143 classified as AB; *middle*: fiber 95, PS; *bottom*: fiber 117, EM+AB.

well as the expected recent star formation in the NGC 4839 group before it fell in (see Zabludoff et al. 1996). This would also explain the large velocity dispersion measured for the emission-line galaxies (Carlberg et al. 1997). We must await further data to fully discriminate between these possible models or others. It is important to note that we only sample galaxies brighter than $b = 18$, and therefore our

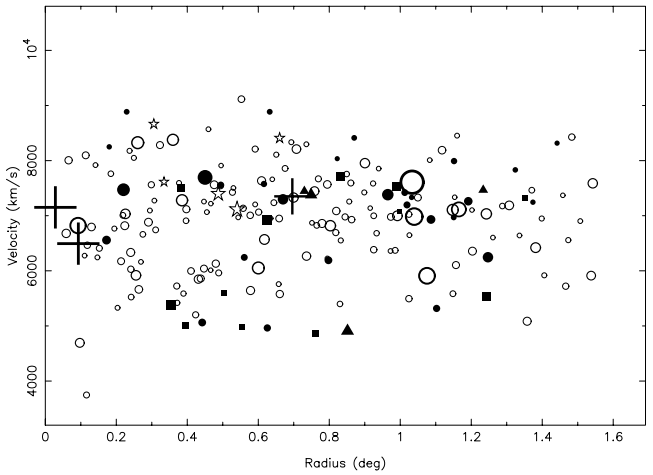


FIG. 19.—Distribution of radial velocities as a function of radius for the observed Coma galaxies. The symbols are the same as in Fig. 3.

observations only apply to the brightest galaxy members and not to the dwarf population (see Rakos et al. 2000). Moreover, our observations do not distinguish between different morphological types (see Doi et al. 1995a, 1995b); this will be addressed using the main SDSS survey data.

The characteristic radius of the Coma cluster is $r_{200} \sim 1.5\ h^{-1}$ Mpc (Geller et al. 1999), or 1°.25, and thus we sample the galaxy population out to the virial radius and slightly beyond. This provides a unique opportunity to study the large-scale star formation histories of galaxies in this nearby cluster. In Figure 20, we present the fraction of passive (absorption) and active (emission plus poststarburst) galaxies as a function of projected distance from the center of Coma. The azimuthally averaged fraction of active galaxies (PS, AB+EM, EM+AB, EM types) appears to increase slightly with radius from 0°.15 to 1°.2,[30] but the observed percentages are also consistent with a constant radial frac-

[30] At the distance of Coma 1° on the sky corresponds to 1.2 h^{-1} Mpc.

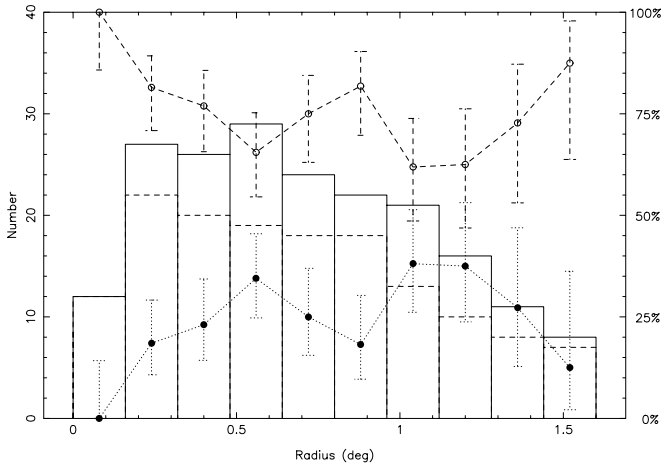


FIG. 20.—Number of observed Coma galaxies (*solid histogram*) and AB type galaxies (*dashed histogram*) as a function of projected radius. The left vertical axis provides the scale. The fraction of old stellar population galaxies (AB; *open circles and dashed line*) and active galaxies (PS, AB+EM, EM+AB, EM; *solid circles and dotted line*) are also plotted. The right vertical axis gives the scale. The errors in the percentages have been computed using the prescription of Gehrels (1986).

tion of active galaxies in this region. This trend is different from that observed in the CNOC sample at higher redshift (Ellingson et al. 2001); i.e., they observe a steeper radial profile for the fraction of active galaxies in their high redshift clusters. However, the results are consistent given the errors and the different analyses performed which render a detailed comparison difficult. Moreover, the target selection used different criteria, although similar, which need to be taken into account to provide a fair comparison.

We find no active galaxies in the central (projected) ~ 200 h^{-1} kpc of the Coma cluster. This result is similar to that observed by Ellingson et al. (2001) who found a deficit of star-forming galaxies within $0.5r_{200}$ of the cores of CNOC1 clusters (see also Rakos et al. 2000 who found a similar trend in intermediate redshift clusters). Ellingson et al. (2001) propose that the dense intracluster medium in the cores of clusters inhibits star formation producing a deficit of star formation compared with the outskirts of the cluster and the general field population. Our data certainly agrees with this scenario except we do see a reduction of active galaxies beyond r_{200}, although this reduction is not statistically significant. We defer a detailed discussion of Coma's star-forming galaxies, and their relation to the X-ray gas, to a future paper.

The Sloan Digital Sky Survey (SDSS) is a joint project of the University of Chicago, Fermilab, the Institute for Advanced Study, the Japan Participation Group, the Johns Hopkins University, the Max Planck Institute for Astronomy, New Mexico State University, Princeton University, the US Naval Observatory, and the University of Washington. Apache Point Observatory, site of the SDSS telescopes, is operated by the Astrophysical Research Consortium. Funding for the project has been provided by the Alfred P. Sloan Foundation, the SDSS member institutions, the National Aeronautics and Space Administration, the National Science Foundation, the Department of Energy, Monbusho, and the Max Planck Society.[31] We acknowledge Michael Strauss for his insightful comments and thank an anonymous referee for his/her helpful comments which have made the paper better.

[31] SDSS can be accessed at www.sdss.org.

REFERENCES

Abraham, R. G., Ellis, R. S., Fabian, A. C., Tanvir, N. R., & Glazebrook, K. 1999, MNRAS, 303, 641
Adami, C., Nichol, R. C., Mazure, A., Durret, F., Holden, B., & Lobo, C. 1998, A&A, 334, 765
Adami, C., Ulmer, M. P., Durret, F., Nichol, R. C., Mazure, A., Holden, B. P., Romer, A. K., & Savine, C. 2000, A&A, 353, 930
Andreon, S., & Ettori, S. 1999, ApJ, 516, 647
Arnaud, M., Aghanim, N., Gastaud, R., Neumann, D., Lumb, D. H., Briel, U. G., Altieri, B., Ghizzardi, S., Mittaz, J., Sasseen, T. P., & Vestrand, W. T. 2001, A&A, 365, L80
Balogh, M. L., Morris, S. L., Yee, H. K. C., Carlberg, R. G., & Ellingson, E. 1999, ApJ, 527, 54
Bernstein, G. M., Nichol, R. C., Tyson, J. A., Ulmer, M. P., & Wittman, D. 1995, AJ, 110, 1507
Biviano, A. 1998, in Untangling Coma Berenices: A New Vision of an Old Cluster, ed. A. Mazure, F. Casoli, F. Durret, D. Gerbal (Singapore: World Sci.), 1
Bromley, B. C., Press, W. H., Lin, H., & Kirshner, R. P. 1998, ApJ, 505, 25
Briel, U. G., Henry, J. P., & Böhringer, H. 1992, A&A, 259, L31
Briel, U. G., et al. 2001, A&A, 365, L60
Burstein, D., Faber, S. M., & González, J. J. 1986, AJ, 91, 1130
Butcher, H., & Oemler, A. 1984, ApJ, 285, 426
Burns, J. O., Roettiger, K., Ledlow, M., & Klypin, A. 1994, ApJ, 427, L87
Caldwell, N., & Rose, J. A. 1997, AJ, 113, 492
Carlberg, R. G., Yee, H. K. C., Ellingson, E., Morris, S. L., Abraham, R., Gravel, P., Pritchet, C. J., Smecker-Hane, T., Hartwick, F. D. A., Hesser, J. E., Hutchings, J. B., & Oke, J. B. 1997, ApJ, 476, L7
Colles, M., & Dunn, A. M. 1996, ApJ, 458, 435 (CD96)
Connolly, A. J., & Szalay, A. S. 1999, AJ, 117, 2052
Connolly, A. J., Szalay, A. S., Bershady, M. A., Kinney, A. L., & Calzetti, D. 1995, AJ, 110, 1071
Doi, M., Fukugita, M., & Okamura, S. 1995a, ApJS, 97, 59
Doi, M., Fukugita, M., Okamura, S., & Turner, E. L. 1995b, AJ, 109, 1490
Dressler, A., & Gunn, J. E. 1983, ApJ, 270, 7
———. 1992, ApJS, 78, 1
Dressler, A., et al. 1999, ApJS, 122, 51
Faber, S. M., Friel, E. D., Burstein, D., & Gaskell, C. M. 1985, ApJS, 57, 711
Ellingson, E., Lin, H., Yee, H. K. C., & Carlberg, R. G. 2001, ApJ, 547, 609
Fan, X., et al. 2001, AJ, 121, 54
Fioc, M., & Rocca-Volmerange, B. 1997, A&A, 326, 950
Folkes, S. R., Lahav, O., & Maddox, S. J. 1996, MNRAS, 283, 651
Folkes, S., et al. 1999, MNRAS, 308, 459
Frieman, J., et al. 2001, in preparation
Fukugita, M., Ichikawa, T., Gunn, J. E., Doi, M., Shimasaku, K., & Schneider, D. P. 1996, AJ, 111, 1748
Galaz, G., & de Lapparent, V. 1998, A&A, 332, 459
Gehrels, N. 1986, ApJ, 303, 336
Geller, M., Diaferio, A., & Kurtz, M. J. 1999, ApJ, 517, L23
Godwin, J. G., Metcalfe, N., & Peach, J. V. 1983, MNRAS, 202, 113 (GMP83)
Honda, H., et al. 1996, ApJ, 473, L71
Horne, K. 1986, PASP, 98, 609
Hughes, J. P. 1989, ApJ, 337, 21
Jacoby, G. H., Hunter, D. A., & Christian, C. A. 1984, ApJS, 56, 257
Kashikawa, N., Sekiguchi, M., Doi, M., Komiyama, Y., Okamura, S., Shimasaku, K., Yagi, M., & Yasuda, N. 1998, ApJ, 500, 750
Kennicutt, R. C. 1992, ApJS, 79, 255
Kent, S. M., & Gunn, J. E. 1982, AJ, 87, 945
Kurtz, M. J., & Mink, D. J. 1998, PASP, 110, 934
Mittaz, J. P. D., Penston, M. V., & Snijders, M. A. J. 1990, MNRAS, 242, 370
Margoniner, V. E., & de Carvalho, R. R. 2000, AJ, 119, 1562
Metevier, A. J., Romer, A. K., & Ulmer, M. P. 2000, AJ, 119, 1090
Neumann, D., et al. 2001, A&A, 365, L74
Nichol, R. C., Collins, C. A., & Lumsden, S. L. 2000, ApJS, submitted (astro-ph/0008184)
Pando, J., & Fang, L.-Z. 1996, ApJ, 459, 1
Poggianti, B. M., Smail, I., Dressler, A., Couch, W. J., Barger, A. J., Butcher, H., Ellis, R. S., & Oemler, A. J. 1999, ApJ, 518, 576
Press, W. H., Teukolsky, S. A., Vetterling, W. T., & Flannery, B. P. 1992, Numerical Recipes in Fortran (Cambridge: Cambridge Univ. Press)
Rakos, K. D., Schombert, J. M., Odell, A. P., & Steindling, S. 2000, ApJ, 540, 715
Rana, N. C., & Basu, S. 1992, A&A, 265, 499
Ronen, S., Aragón-Salamanca, A., & Lahav, O. 1999, MNRAS, 303, 284
Sodré, L., & Cuevas, H. 1997, MNRAS, 287, 137
Thompson, R. I., Weymann, R. J., & Storrie-Lombardi, L. J. 2001, ApJ, 546, 694
Theuns, T., & Zaroubi, S. 2000, MNRAS, 317, 989
Uomoto, A., et al. 2001, in preparation
Wang, Q. D., Connolly, A., & Brunner, R. 1997, ApJ, 487, L13
West, M. J. 1998, in Untangling Coma Berenices: A New Vision of an Old Cluster, ed. A. Mazure, F. Casoli, F. Durret, & D. Gerbal (Singapore: World Sci.), 36
White, S. D. M., Briel, U. G., & Henry, J. P. 1993, MNRAS, 261, L8
Worthey, G. 1994, ApJS, 95, 107
York, D. G., et al. 2000, AJ, 120, 1579
Zabludoff, A. I., Zaritsky, D., Lin, H., Tucker, D., Hashimoto, Y., Shectman, S. A., Oemler, A., & Kirshner, R. P. 1996, ApJ, 466, 104